KINEMATICS ANALYSIS OF LARAMIDE DEFORMATION IN NORTH-CENTRAL NEW MEXICO

A Thesis

Presented to

the Faculty of the Department of Earth and Atmospheric Sciences

University of Houston

In Partial Fulfillment

Of the Requirements for the Degree

Master of Science

By

Hongge Kan

December 2012

KINEMATICS ANALYSIS OF LARAMIDE DEFORMATION

IN NORTH-CENTRAL NEW MEXICO

_____

Hongge Kan

APPROVED

_____

Dr. Alexander Robinson

_____

Dr. Michael Murphy

_____

Dr. Ran Zhang

_____

Dean, College of Natural Sciences and Mathematics

ACKNOWLEDGEMENTS

I express gratitude to Dr. Alexander Robinson for his direction and supervising this thesis. Dr. Robinson's attitude towards knowledge and his patience to students taught me what a real geologist and professor is, and will influence me for the rest of my life. I also thank Dr. Murphy for his help and directions. I think he always brought much optimism and happiness to the people around him. I thank Dr. Zhang's suggestion on my career and further study of Geology. I also appreciate my friends An Li and Yiduo Liu who always cared about my research and shared their sharp opinions with me. I am thankful for the support of my parents who never give up on me.

KINEMATICS ANALYSIS OF LARAMIDE DEFORMATION IN NORTH-CENTRAL NEW MEXICO

An Abstract of a Thesis

Presented to

the Faculty of the Department of Earth and Atmospheric Sciences

University of Houston

In Partial Fulfillment

Of the Requirements for the Degree

Master of Science

By

Hongge Kan

December 2012

ABSTRACT

Deformation related to the Late Cretaceous-Early Eocene Laramide orogeny in north-central New Mexico resulted in the formation of the Nacimiento uplift, Gallina uplift, and corresponding faults. In the past thirty years the nature of Laramide deformation has remained highly debated with kinematic models including single-stage NE-SW to E-W-directed shortening, multiphase-multidirectional shortening, and NNE-SSW-directed transpressive deformation.

However, in recent years a growing body of evidence indicates that the Laramide orogeny in northern New Mexico was dominated by ~E-W horizontal shortening and compression. One key in resolving local structural models is to understand along strike variations in the magnitude of shortening along the Nacimiento-Gallina uplifts. Based on gravity modeling, Pollock et al. (2004) interpreted the high-angle E-dipping Nacimiento fault to root into a gently dipping master fault and calculated an E-W component of shortening of ~7 km. In this study, I used formation boundary elevations from well data in the adjacent San Juan basin and geologic maps of the Nacimiento and Gallina uplifts to construct a 3D geologic model of formation surfaces across the structures. I then modeled their formation as fault propagation folds in the program Move, to make estimates of the fault geometry and the E-W shortening across the uplifts. Based on forward models, the subsurface geometry of the structures responsible for the uplifts includes a gently (~25 °) E-dipping master fault and a high-angle (~70 °) E-dipping fault beneath the Gallina uplift, similar to the structures documented along the central Nacimiento uplift. My modeling suggests the initial tip of the high-angle fault is on the master fault, indicating it branches

from it. At the northern end of the Nacimiento uplift, the total shortening accommodated by slip along the master fault and Nacimiento fault is ~5.3 km. To the north the total shortening decreases to ~4.3 km where the high-angle Nacimiento fault is blind under the Gallina uplift. This study does not support the prediction of Hamilton (2009) that significant E-W shortening was transferred from the northern end of the Nacimiento uplift to the Tusas uplift to the east via a diffuse transpressional zone.

CONTENTS

1. Introduction

The Late Cretaceous-Early Eocene Laramide orogeny was a period of mountain building in western North America related to eastward subduction of the Kula and Farallon plates under the North American plate. Laramide deformation in north-central New Mexico resulted in the formation of the Nacimiento uplift, Gallina uplift, and corresponding faults (Figure 1). Over the past thirty years there has been significant debate about the kinematics of Laramide deformation. This has resulted in several different hypotheses including: 1) single-stage NE-SW to E-W-directed shortening (Yin and Ingersoll, 1997; Erslev and Koening, 2009), 2) sequential multidirectional shortening (Erslev, 2001), and 3) transpressive deformation partitioned between NW-SE-striking thrust and N-S-striking strike-slip faults (Chapin and Cather, 1981; Chapin, 1983; Laughlin et al., 1983; Karlstorm and Daniel, 1993; Cather et al., 2006). However, in recent years most studies have concluded that the Laramide orogeny was dominated by NE-SW to E-W-directed horizontal shortening and compression. Erslev and Koening (2009) calculated an average Laramide slip and maximum compressive stress direction of N67E for the Rocky Mountain and argued these largely unimodal, subhorizontal slip and compression directions varied only slightly in space.

Based on the growing consensus of E-W-directed horizontal shortening and compression, Hamilton (2009) proposed an E-W-trending 'Accommodation Zone' of strike-slip deformation from the northern Nacimiento uplift to the southern Tusas Mountains along which much of the strain on the Nacimiento uplift was transferred northeastward to the Tusas Mountains (Figure 1). Davis (2010) tested this model by

calculating the change in the amount of shortening across the bend area in topography between the Nacimiento uplift and the Gallina uplift based on line-balanced calculations which indicated an abrupt change in shortening from the Nacimiento uplift (~5 km) to the Gallina uplift (~1 km). The calculated shortening along the Nacimiento uplift was similar to the south. Pollock et al. (2004) calculated ~7 km of the E-W shortening along the central portion of the Nacimiento uplift based on balanced cross sections. Further, their work interpreted the high-angle Nacimiento fault to root into a blind low-angle master fault based on field and gravity data.

One important observation is that the orientation of strike-slip deformation in the 'Accommodation Zone' from Hamilton (2009) is the same as Erslev and Koening's (2009) average Laramide slip and maximum compressive stress direction of N67E for the Rocky Mountains. It is also the same as the orientation of the Tijeras-Canoncito strike-slip fault (Figure 1) which was interpreted to indicate the direction of Laramide compression by Yin and Ingersoll (1997). The Tijeras-Canoncito fault is the southern boundary of an interpreted 'Pop-up' structure by Yin and Ingersoll (1997) which is defined by the Nacimiento uplift to the west, Sangre de Cristo uplift to the east.

In this study, I use the elevation of geologic contacts from well data in the adjacent San Juan basin to the west and the elevation of the same contacts from geologic maps along the Nacimiento-Gallina uplifts to construct 3D models of several formation contacts across the northern Nacimiento uplift and the Gallina uplift with the software ArcGis and Move. Based on forward modeling of cross sections through these structures using the trishear kinematic model, I test the interpreted subsurface geometry beneath the

Nacimiento uplift by Pollock et al. (2004) and predict the subsurface geometry beneath the Gallina uplift. Based on these interpreted subsurface geometry, the E-W shortening from the northern end of the Nacimiento uplift to the Gallina uplift is calculated to test the 'Accommodation Zone' model of Hamilton (2009) which proposed much of the strain on the Nacimiento uplift was transferred northeastward to the Tusas Mountains.

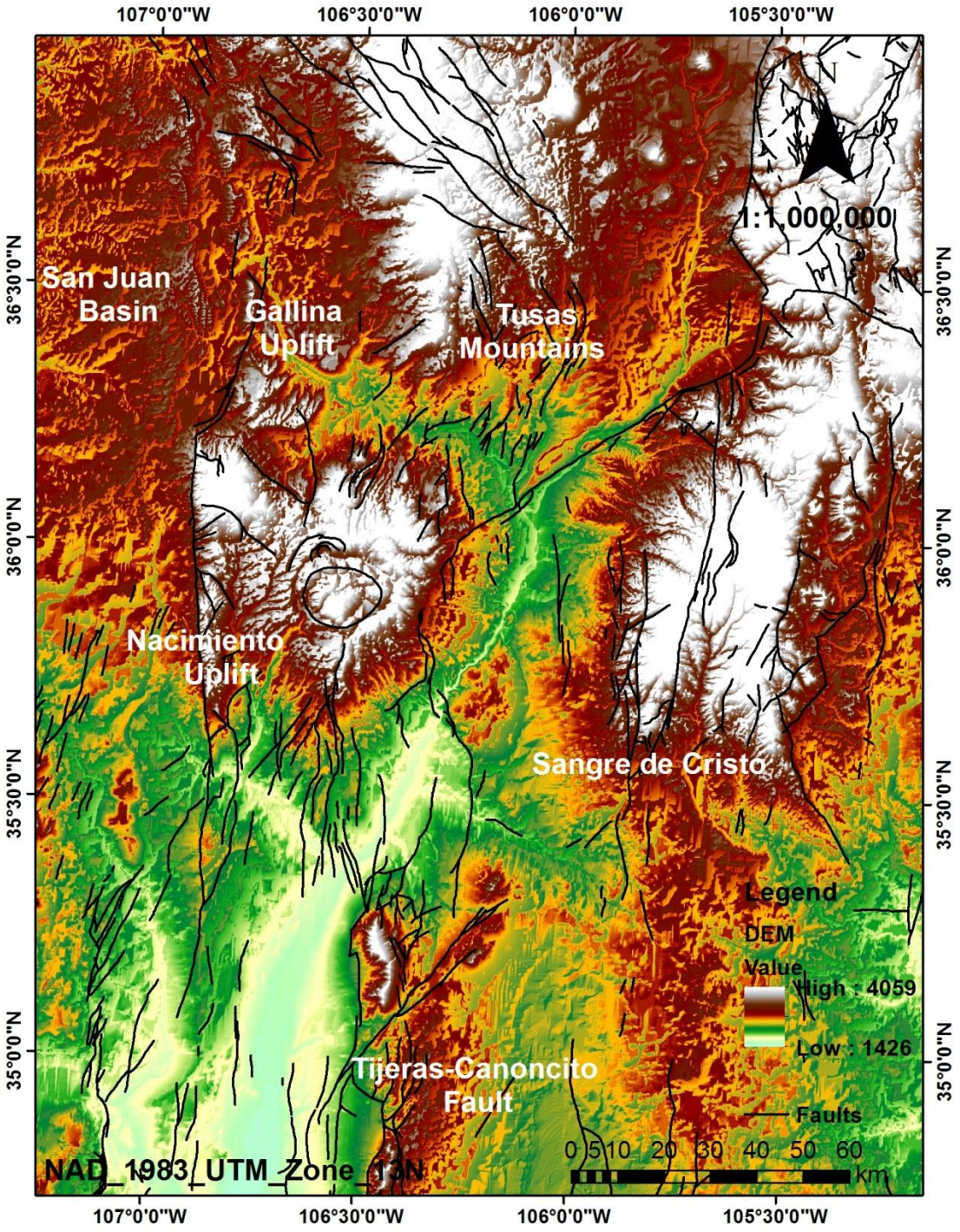

Figure 1. DEM map showing the Nacimiento uplift, Gallina uplift, Tusas Mountains, Sangre de Cristo uplift, and Tijeras-Canoncito fault.

2. Tectonic History and Regional Models

2.1 Tectonic History

The Western Cordillera of North America has a protracted tectonic history. North-central New Mexico encompassed part of the regional Paleoproterozoic suture zone between the 1.76-1.72 Ga Yavapi Province and the 1.7-1.6 Ga Mazatzal Province. Suturing of these provinces occurred during the ca. 1.65 Ga Mazatzal orogeny (Karlstrom and Daniel, 1993). Seven major tectonic events have subsequently modified the crust in the study area including a ca. 1.45-1.35 Ga magmatic and orogenic event, the ca. 1.1 Ga Grenville orogeny, the ca. 0.7 Ga rifting of western Rodinia, Cambrian extension and magmatism related to the southern Oklahoma aulacogen, the Late Paleozoic Ancestral Rocky Mountain orogeny, the Late Cretaceous-Eocene Laramide orogeny, and Oligocene-Holocene extension related to the Rio Grande rift (Cather et al., 2006).

The Laramide orogeny was a period of mountain building and magmatism in western North America, which started in the Late Cretaceous, 70 to 80 million years ago, and ended 35 to 55 million years ago. Laramide deformation was the result of the eastward subduction of the Kula and Farallon plates under the North American plate. Because little coeval magmatism occurred throughout the central Rockies, most hypotheses proposed that the angle of subduction was shallow. The Laramide orogeny produced numerous intermontane structural basins and adjacent mountains in what had been the foreland of the Sevier orogeny (DeCelles, 2004). Today, Laramide structural uplifts are typically bound by thrust or reverse faults although many are blind creating monoclines at their margins.

Age constraints on Laramide tectonic deformation are mainly based on the sedimentary successions of the nearby basins. These successions mainly consist of three parts, including the middle Campanian-early Maastrichtian, latest Maastrichtian-middle Paleocene, and Eocene which are separated by regional unconformities in New Mexico. The stratigraphic record in basins allows relatively precise ages and magnitudes to be assigned to subsidence events. Another technique of dating exhumation events is apatite fission track (AFT) thermochronology, which dates the time of cooling through ~80 to ~120 ℃ and can evaluate the approximate time and rate of uplift and exhumation independent of the stratigraphic record in adjacent basins. While the age of Laramide tectonism is debated, there is a consensus on its initiation in the late Cretaceous and its cessation in the Eocene. Cather (2004) argued that initiation of uplift started in the early Campanian (~95-78 Ma) and ended at the late Eocene (~36 Ma) with the onset of volcanic transitions brought on by the Rio Grande rift. DeCelles (2004) argued that the Laramide did not begin until approximately 80 Ma with the peak of Laramide deformation and uplift occurred between the Maastrichtian to early Eocene (~71-55 Ma).

Laramide deformation in north-central New Mexico produced the Nacimiento uplift, Gallina uplift, Brazos uplift, San Juan basin, Chama basin, and related fault systems (Figure 2). To systematically evaluate the evolution of Laramide uplifts, Cather (2004) compiled a list of criteria that correspond to sequential stages of uplift development. Most criteria are derived from the sedimentary records in adjacent basins. In the criteria, Cather (2004) proposed: (1) the initial stage of Laramide uplift development was recorded in the Cenomanian-early Campanian age (-95-78 Ma) strata

with sedimentary aggradation related to regional foreland subsidence; (2) incipient Laramide intraforeland deformation caused increased sedimentation rates during the Campanian (~78-71 Ma) in the axial part of the San Juan basin; (3) continued deformation resulted in areas of mild erosion over nascent Laramide uplifts and initial AFT cooling age (>74 Ma); (4) continuous rise of Laramide uplifts exposed older strata that contribute petrologically distinctive and locally derived detritus to adjacent basins; (5) culminate Laramide orogeny deformation was characterized by widespread erosion of Paleozoic and Precambrian rocks from uplifted areas and rapid deposition of locally sourced clastics in intraforeland basins; (6) waning Laramide deformation continued during widespread, intermediate composition volcanism; (7) the Laramide orogeny ended with the beginning of extensional tectonism which resulted in bimodal volcanism and incipient structural inversion of Laramide uplifts. This study mainly focuses on the formation of the Nacimiento uplift and the Gallina uplift during the Laramide. The amount of the E-W shortening is calculated along the Nacimiento-Gallina uplifts to test the different kinematic hypotheses based on the detailed interpretation of the subsurface geometry under the uplifts from the trishear kinematic model.

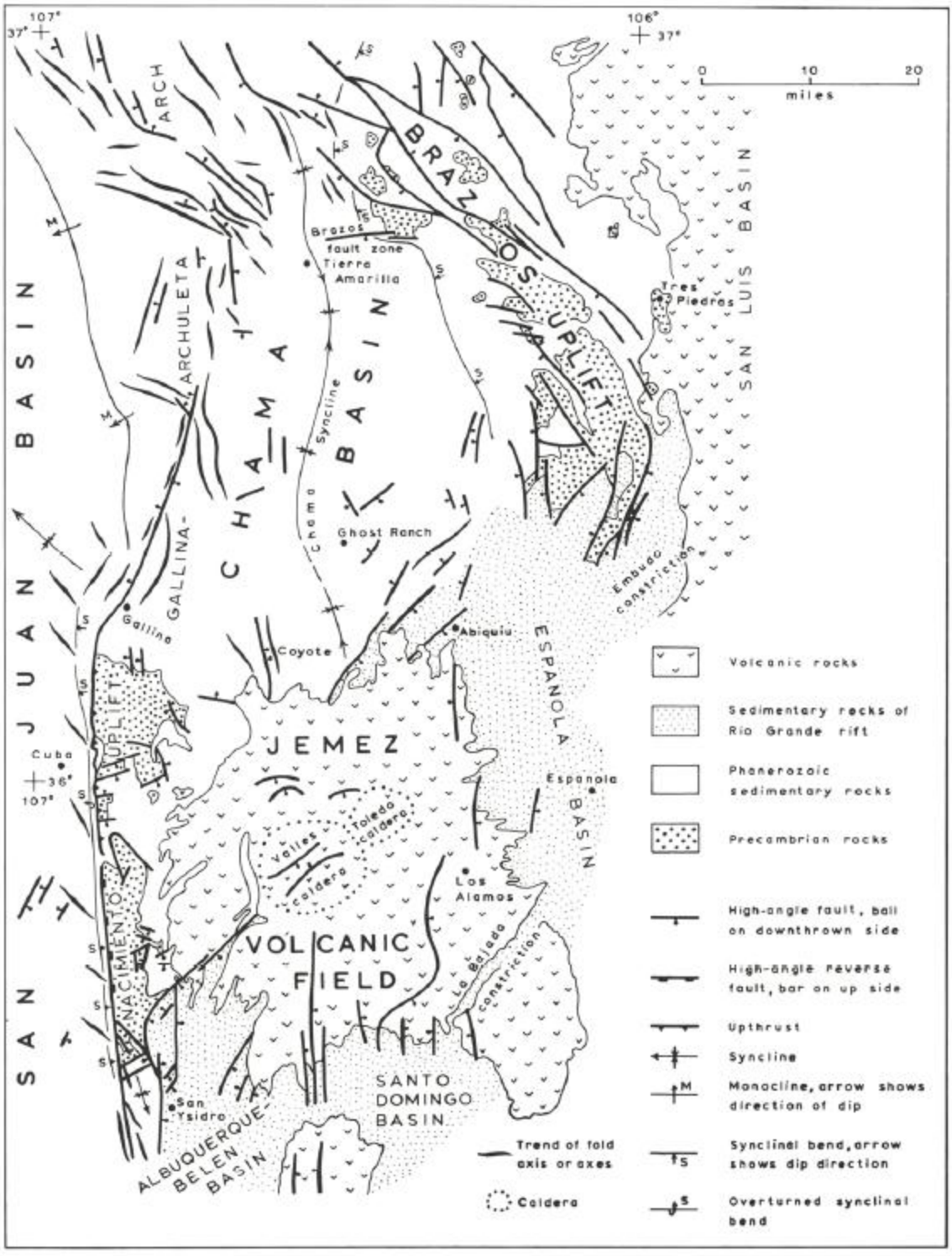

Figure 2. Generalized tectonic map of north-central New Mexico showing Laramide uplifts, basins, and related structures (Woodward, 1974).

2.2 Large Dextral Slip Models

The kinematics of Laramide deformation along the southern Rocky Mountains in Colorado and northern New Mexico is a subject of debate with kinematic models including: 1) a single-stage of NE-SW to E-W-directed shortening, 2) sequential multidirectional shortening, and 3) transpressive deformation partitioned between NW-SE-striking thrust faults and N-S-striking strike-slip faults. This debate is mainly the result of the general steepness and linear trace of the Nacimiento fault, as well as the en echelon series of northwest-plunging growth folds in the San Juan basin (Figure 1 and 2). This led to the interpretation that Laramide deformation in north-central New Mexico resulted from transpression with a large dextral component of displacement (Chapin and Cather, 1981; Chapin, 1983; Laughlin et al., 1983; Karlstorm and Daniel, 1993; Cather, 2004; Cather et al., 2006).

Karlstorm and Daniel (1993) estimated ~25 km of dextral displacement based on offset of aeromagnetic anomalies across the Nacimiento fault system, which they attributed largely to Laramide deformation. Cather (2004) used the calculated ~7 km from Pollock et al. (2004) as the E-W component of shortening between the San Juan basin and the Nacimiento uplift and calculated ~16.5 km (7 km/sin20°) of dextral separation for the Gallina fault and ~15 km (7 km/cos20°) of dextral separation for the Nacimiento fault (Figure 3). In his model the compressive direction is represented by the orientation of the Gallina fault (N20E), with the Gallina fault interpreted as a dextral strike-slip fault with large displacement. The biggest problem with this model is that the predicted E-W component of shortening along the Gallina uplift is almost zero so the

model cannot explain the formation of the Gallina uplift. Further, this model is inconsistent with Erslev and Koening's (2009) interpreted slip and maximum compressive stress direction (N67E) for the Rocky Mountains.

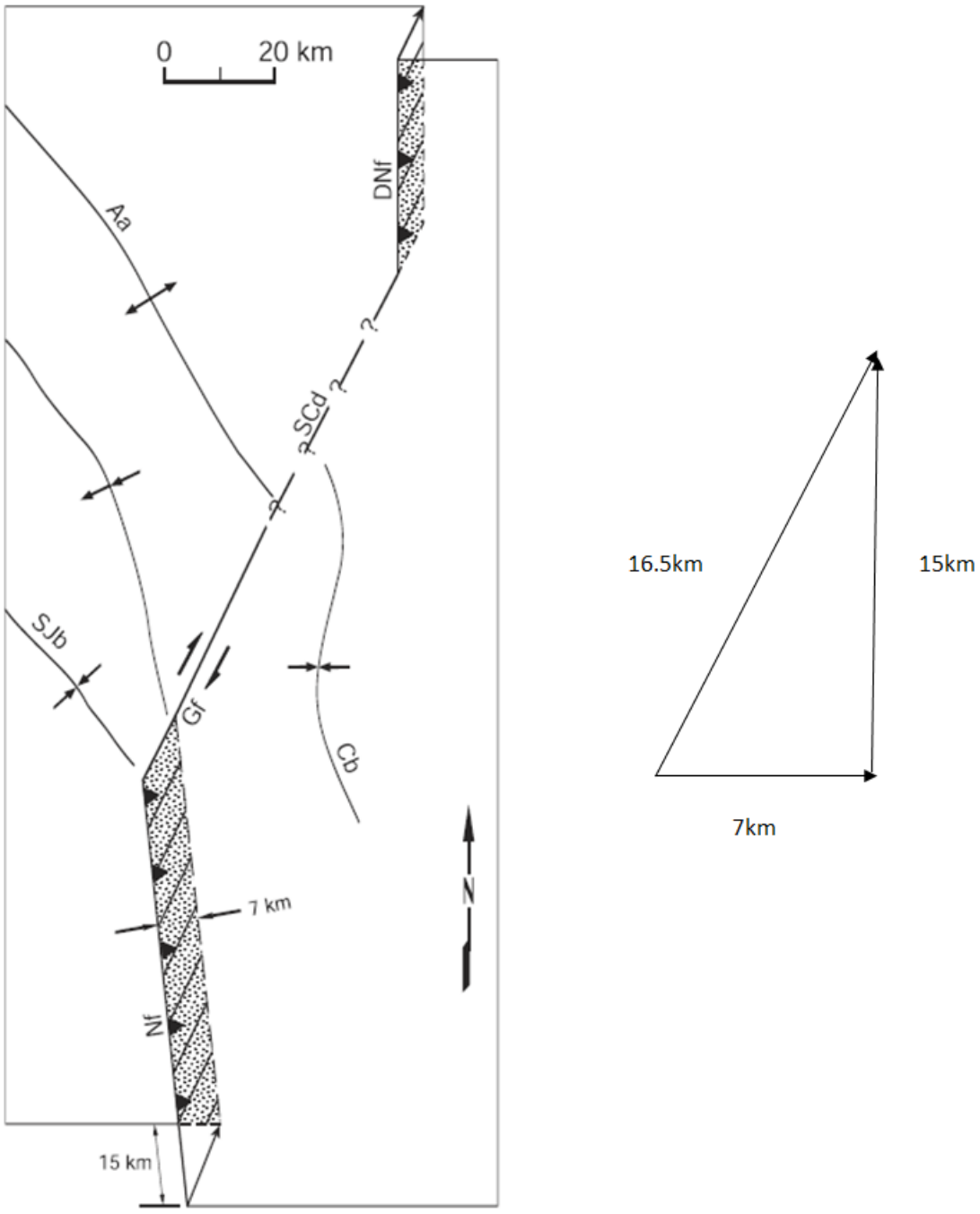

Figure 3. Simplified tectonic models for Laramide development of Nacimiento-Gallina uplifts. DNf, Del Norte fault; Aa, Archuleta Anticlinorium; SCd, Salado-Cumbres discontinuity; SJb, axis of San Juan basin; Gf, Gallina fault; Cb, Chama basin; Nf, Nacimiento fault. Modified from Cather (2004).

2.3 Single-stage NE-SW to E-W-directed Shortening Models

Some researchers have questioned whether significant offset occurred during Laramide deformation (Yin and Ingersoll, 1997; Woodward et al., 1997; Pollock et al., 2004). Woodward et al. (1997) pointed out the aeromagnetic anomalies are located in Proterozoic rocks and therefore likely predate the Laramide orogeny. He estimated 5 to 20 km of the dextral slip since Laramide. More recently, Pollock et al. (2004) interpreted the amount of dextral strike-slip motion on the Nacimiento fault system to be between 3 km and 15 km and suggested the strike-slip motion occurred before the main episode of Laramide shortening. Pollock et al. (2004) suggested the dextral offset was instead related to Proterozoic deformation, the late Paleozoic Ancestral Rocky mountain orogeny, or an early phase of Laramide deformation.

Yin and Ingersoll (1997) interpreted the Laramide uplifts and basins as the direct response to rapid NE-SW convergence between the North American and Farallon plates, without multiple reorientations of Laramide stress fields and without major strike-slip displacement along the eastern side of the Colorado Plateau (Figure 4). They divided the Laramide faults in the southern Rocky Mountain into an E-dipping thrust system and a W-dipping thrust system. In their model, the E-dipping Nacimiento fault was interpreted as the back-thrust of the W-dipping Sangre de Cristo system to the east. Yin and Ingersoll (1997) interpreted the Laramide compressional direction to be parallel to the NE-SW trend of the Tijeras-Canoncito fault. Their proposed Laramide compressional direction is consistent with the interpreted average Laramide slip and maximum compressional direction of N67E from Erslev and Koening (2009).

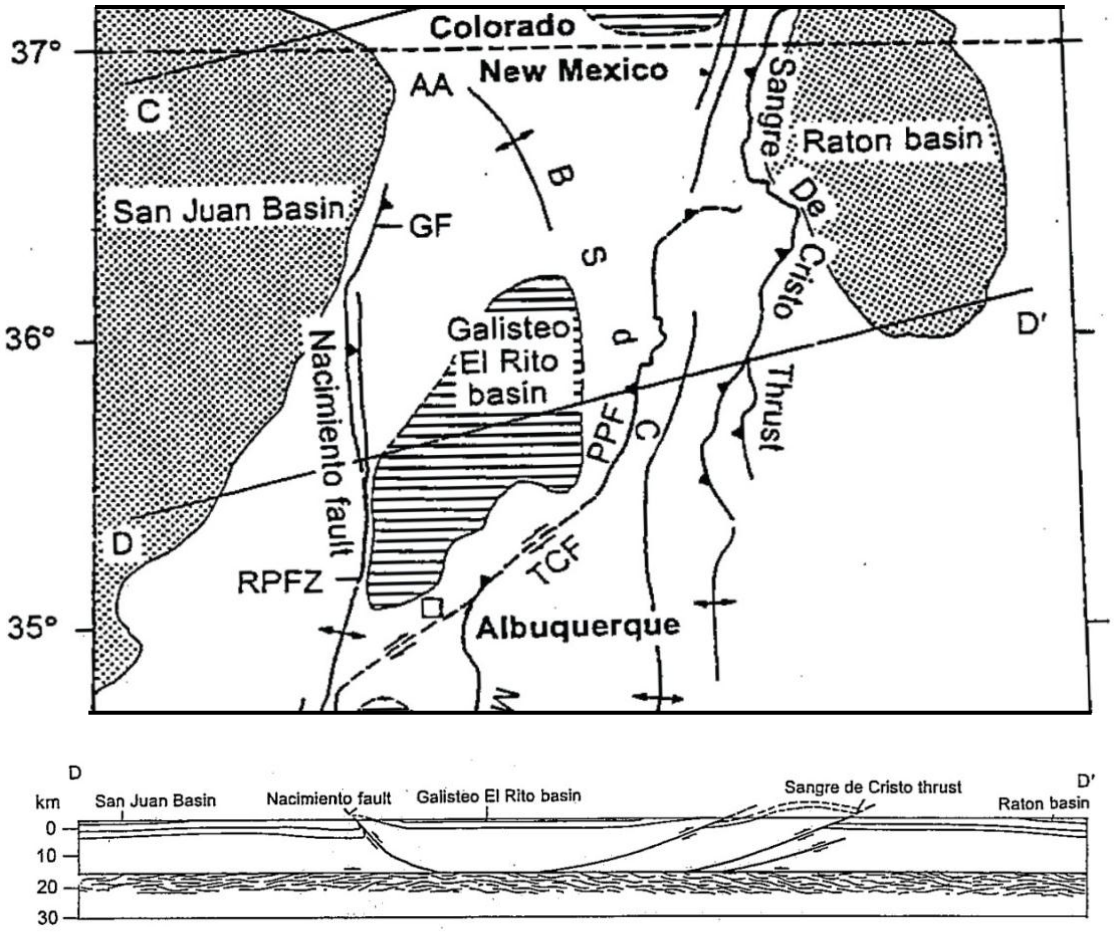

Figure 4. Tectonic model of the Nacimiento uplift showing directly NE-SW convergence. AA, Archuleta Arch; GF, Gallina Fault; PPF, Rio Puerco Fault Zone; TCF, Tijeras-Canoncito Fault; SLU, Sierra-Ladron Uplift; BSdC, Brazos Sangre de Cristo uplift. Modified from Yin and Ingersoll (1997).

2.4 Sequential Multidirectional Shortening Models

Erslev (2001) argued for a multiphase and multidirectional deformation history during the Laramide based on multimodal slickenline and ideal σ_1 orientations, as well as crosscutting relationship. In his study, 2552 minor faults were measured at 88 localities throughout north-central New Mexico. Localities with rocks older than the Pennsylvanian-Permian Sangre de Cristo Formation were not measured due to the possible presence of faults related to the Paleozoic ancestral Rocky Mountain orogeny and earlier tectonism. Similarly, localities exposing Neogene rocks were not considered because they were presumed only to record Rio Grande rift faulting. He proposed the early Laramide E-W thrusting formed N-S-trending Laramide arches and later that counterclockwise rotation of regional shortening may have caused transpression.

In his model, the minor fracture data was interpreted to show the Laramide horizontal shortening and compression occurred at an oblique angle to the Nacimiento fault system (Figure 5). The lack of a large population of N-S-striking right-lateral faults suggested that the Nacimiento fault system was not dominated by strike-slip motion (Erslev, 2001). In the Nacimiento uplift, rose diagrams of slickenline trends from thrust faults show a unimodal trend, averaging N71E. However, in the Gallina uplift the rose diagrams of ideal σ_1 axis show a broad distribution between E-W and NE-SW trends, indicating two distinct directions of horizontal shortening and compression.

However, Erslev and Koening (2009) changed previous interpretations of distinct kinematic phases, and instead concluded that the interpreted multidirectional Laramide

deformation was the result of the combination of local unimodal domains, not regionally pervasive bimodal distribution.

Hamilton (2009) mapped an area between the Nacimiento and Tusas Mountains in the Abiquiu area. In his study the fold geometry coupled with fault and fractures patterns suggested multiple compression directions. He interpreted a counter-clockwise rotation (~65 °) of σ_1 as Laramide deformation progressed. He also proposed a multistage 'Accommodation Zone' model in which much of the strain on the Nacimiento uplift was transferred northeastward to the Tusas Mountains along an E-W-trending zone of strike-slip deformation.

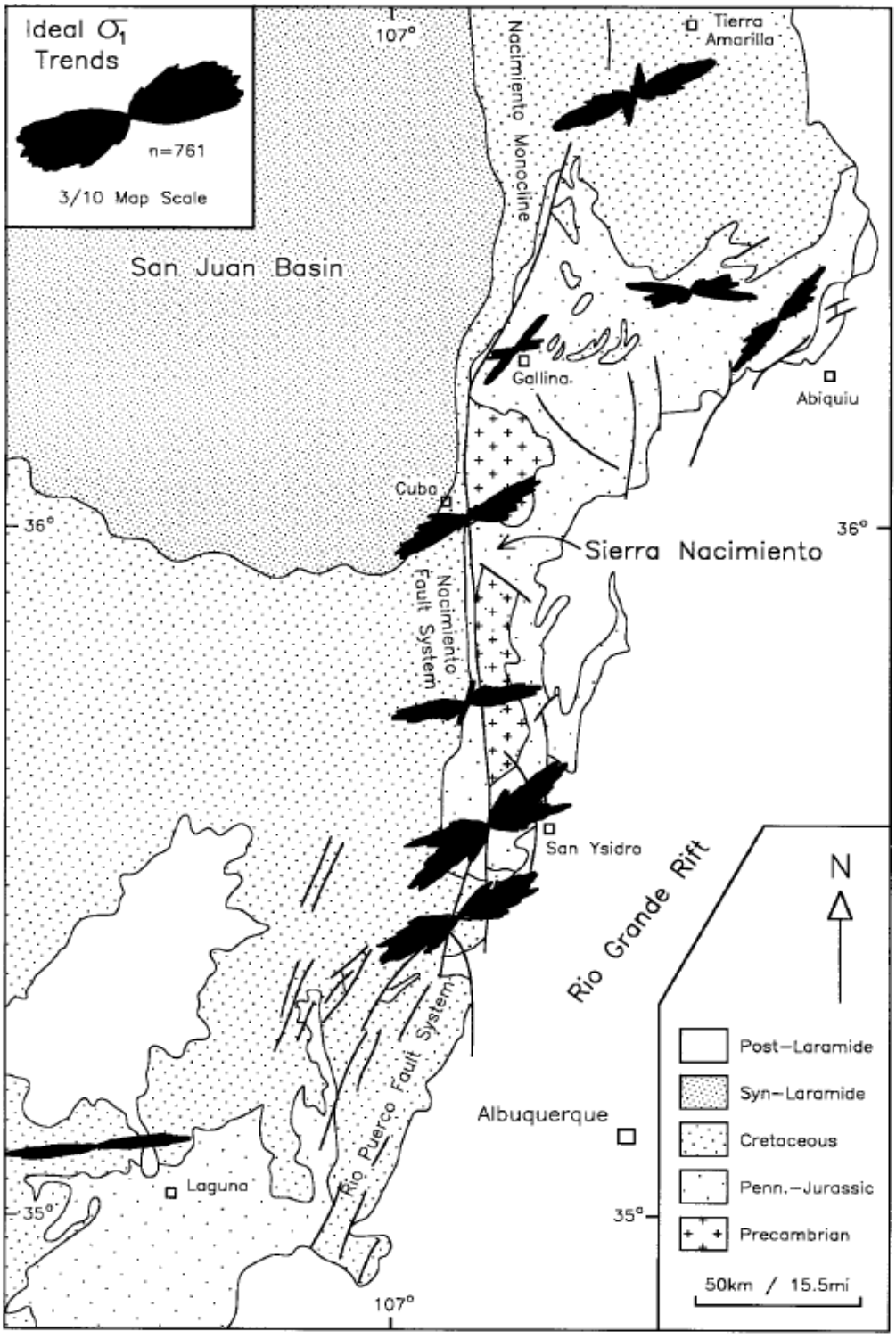

Figure 5. Fault data expressed as smoothed rose diagrams of ideal σ_1 trends for the Nacimiento and Gallina uplifts (Erslev, 2001).

3. Geologic Structures of the Nacimiento and Gallina Uplifts

3.1 Nacimiento Uplift

The Nacimiento uplift extends for approximately 80 km in length and is 10 km to 16 km wide (Figure 1). In general, it consists of an uplifted block of largely Proterozoic to Paleozoic lithologies which is tilted eastward and is bound to the west by faults. Structural relief is at least 3 km, although a significant part of this is attributable to a late Paleozoic precursor, the Penasco uplift (Woodard, 1996). To the east, the Nacimiento uplift is bound by the post-Laramide Rio Grande rift and the Jemez Volcanic field.

To the west of the Nacimiento uplift, a series of en echelon northwest-plunging growth folds in the San Juan basin have been interpreted to be related to dextral components of slip on the range-bounding fault (Kelley, 1955; Baltz, 1967). The Nacimiento uplift terminates to the south with folds that plunge to the south beneath an unconformable cover of Cenozoic rocks (Slack et al., 1976). The northern end of the uplift is a broad, faulted anticline that plunges 10 °to 20 °northward and merges with the Gallina-Archuleta arch (Woodward, 1974). The northeastern part of the uplift connects with the Chama basin through a broad syncline.

The earliest stratigraphic evidence for Laramide uplift of the Nacimiento uplift is the thinness or absence of the late Campanian (~75 Ma) Pictured Cliffs Sandstone in the steeply dipping to overturned eastern limb of the basin-margin syncline that parallels the Nacimiento fault to the west (Baltz, 1967; Fassett and Hinds, 1971; Woodward, 1987). The oldest AFT cooling age in the Nacimiento uplift is Campanian (80.8 ± 7.5 Ma.) with most of the remaining cooling ages Paleocene and Eocene (Kelley et al., 1995)

3.2 Nacimiento Fault

The Nacimiento fault strikes north to south along the western flank of the Nacimiento uplift. The term Nacimiento fault is used to denote the continuous western structural boundary of the Nacimiento uplift (Cather, 2004). The western boundary fault system of the Nacimiento uplift was initially interpreted to consist of two faults (Pajarito and Nacimiento faults) that were separated along strike by a gap in which unfaulted Permian strata are exposed (Woodward, 1987; Woodward et al., 1992; Woodward, 1996). However, Pollock et al. (2004) demonstrated that faulting is continuous through the gap based on field mapping.

Kinematic interpretations of the Nacimiento fault system are varied and include: 1) a back-thrust (Yin and Ingersoll, 1997), 2) vertical dipping reverse fault (Woodward, 1987), and 3) right-lateral strike-slip fault (Karlstrom and Daniel, 1993; Cather, 1999). The variety in interpretation is due in part to the exposed faults along the western side of the Nacimiento uplift which include high-angle reverse faults, low-angle reverse faults, high-angle normal faults, and strike-slip faults (Renick, 1931; Baltz, 1967; Woodward, 1976; Woodward, 1987).

Based on field mapping and gravity modeling, Pollock et al. (2004) interpreted the Nacimiento uplift to be a result of horizontal shortening along a low-angle blind thrust fault as well as an exposed high-angle reverse fault. They interpreted the exposed high-angle Nacimiento fault to sole downward into a gently E-dipping master thrust fault, the tip of which is blind and lies beneath the Phanerozoic strata of the San Juan basin

(Figure 6). Based on their model, Pollock et al. (2004) calculated an E-W component of shortening of ~7 km.

High-angle thrust faults in the sedimentary cover along the western margin of the uplift have been mapped by Woodward (1987), Stewart and Hibbard (1992), and Giral (1995), as well as earlier workers. Stewart and Hibbard (1992) identified a low-angle thrust fault in the sedimentary cover that they interpreted as an early structure that preceded the main stages of uplift. However, Pollock et al. (2004) argued these low-angle faults may be the result of temporally distinct tectonic events during the Laramide. They also pointed out the strata in the eastern San Juan basin to be tightly folded and form a monocline adjacent to the Nacimiento uplift.

Based on field work, Pollock et al. (2004) observed structural thinning of the sedimentary units (e.g., Todilto formation and the shale members of the Chinle formation) adjacent the Nacimiento uplift. Also, on the geologic map of Regina quadrangle by Merrick and Woodward (1982), the sedimentary bedding adjacent the high-angle Nacimiento thrust fault changes from steeply dipping to overturned to the south. Based on these observations, I used the trishear kinematic model to interpret the formation of these fault propagation monoclines as it allows thinning and overturning of strata, whereas the kink-band method of modeling fault propagation folds does not.

At the northern end of the Nacimiento uplift, the exposed N-S-striking Nacimiento high-angle reverse fault connects with ENE-WSW-striking high-angle faults (Figure 7). The ENE-WSW-striking high-angle faults mainly consist of two faults in the bend area. The eastern fault connects with the Nacimiento fault and the western fault

connects with the Gallina fault which extends along the Gallina uplift. Their strike direction is consistent with the slip direction and the maximum stress direction (N67E) for the Rocky Mountains interpreted by Erslev and Koening (2009). Further, the ENE-WSW-striking faults occur at a bend in topography between the Nacimiento uplift and the Gallina uplift and parallel the shear structures in both the 'Accommodation Zone' (Figure 8) from Hamilton (2009) and the Tijeras-Canoncito strike-slip fault interpreted to indicate the Laramide compressional direction by Yin and Ingersoll (1997).

The interpreted 'Accommodation Zone' from Hamilton (2009) is an area between the northern end of the Nacimiento uplift and the southern end of the Tusas Mountains (Figure 8). Hamilton (2009) collected data from strike-slip faults and fractures from the Triassic Chinle Formation and the Permian Culter Formation and documented their orientation as parallel to the Tijeras-Canoncito strike-slip fault at the southern boundary of the axial basin between the Nacimiento uplift and the Sangre de Cristo uplift. He interpreted significant E-W shortening was transferred from the northern end of the Nacimiento uplift to the Tusas uplift to the east through his observed shear structures.

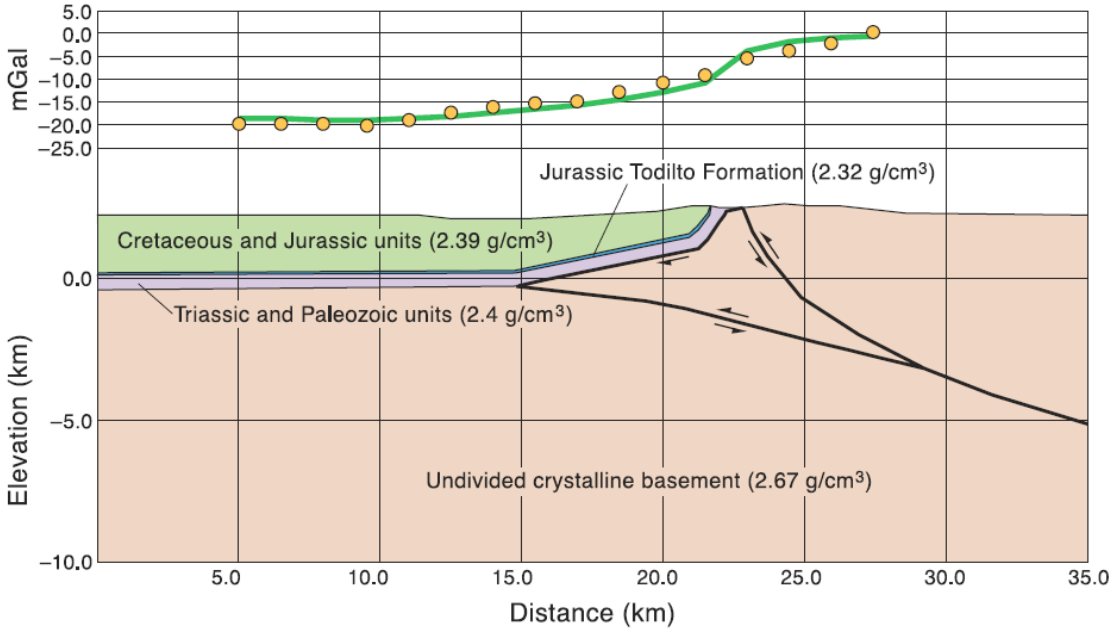

Figure 6. Gravity and structural models of the eastern San Juan basin and Nacimiento uplift. Circles are the measured complete Bouguer anomaly values; the solid line is the complete Bouguer anomaly profile calculated from geologic model (Pollock et al., 2004).

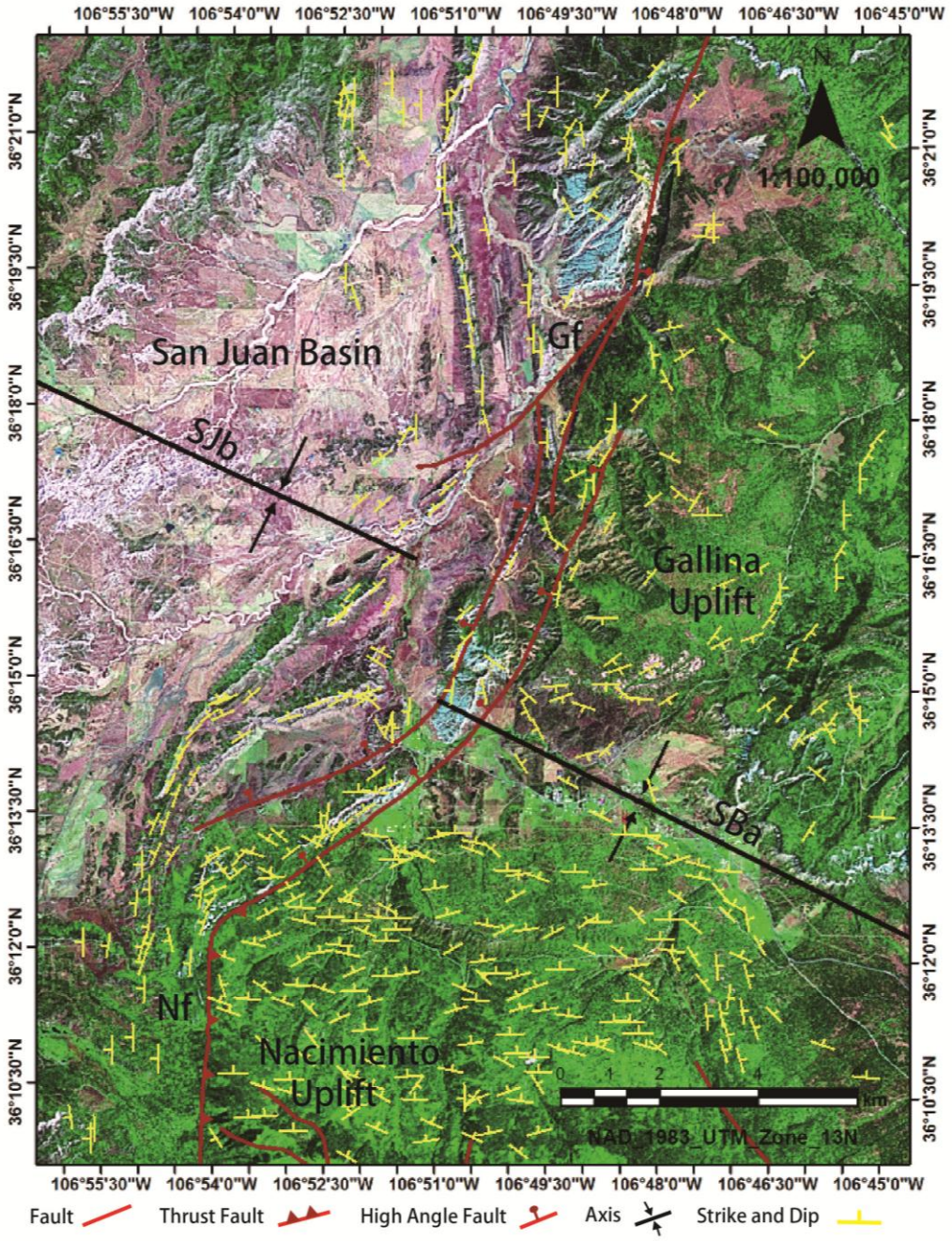

Figure 7. Map of the bend area between the Nacimiento uplift and the Gallina uplift showing the N-S-striking Nacimiento reverse fault, ENE-WSW-striking high-angle fault, Gallina fault, and the axis of the San Juan basin and a syncline on the east side; the location of the axis in the San Juan basin from the published structural map (Cather,2004). SBa, axis of the bend area; SJb, axis of the San Juan basin; Gf, Gallina fault; Nf, Nacimiento fault.

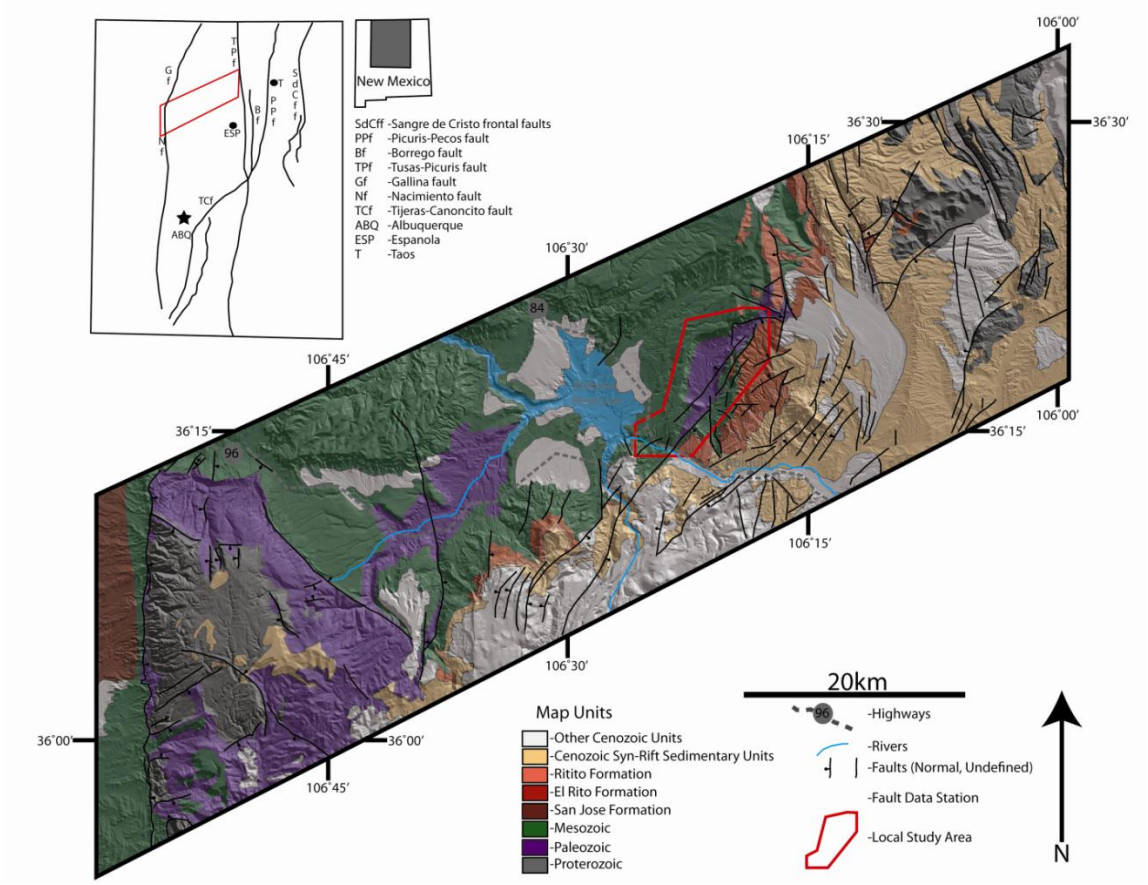

Figure 8. Map of the 'Accommodation Zone' showing the shear structures paralleled the Tijeras-Canoncito strike-slip fault (Hamilton, 2009).

3.3 Gallina Uplift

To the north, the Nacimiento uplift connects with the Gallina uplift across a right-lateral bend in the topography (Figure 7). The Gallina uplift is the southern part of the Gallina-Archuleta arch (Kelley and Clinton, 1960) and is ~40 km in length and up to ~12 km wide. Structural relief measured from the top of the Cretaceous Dakota Sandstone between the uplift and the San Juan basin to the west is ~2.5 km (Woodward, 1992).

The Gallina-Archuleta arch extends 150 km from the Nacimiento uplift to Hogback monocline in Southern Colorado (Woodward, 1974; Woodward, 1987). In general the Gallina-Archuleta arch is a N-S-trending, arcuate anticlinorium which separates the relatively deep San Juan basin to the west from the Chama basin to the east (Figure 1 and 2). The western flank of Gallina-Archuleta arch consists of a monocline along the eastern boundary of San Juan basin and the eastern margin of the arch merges with the shallow Chama basin through a broad, E-dipping slope which is the western limb of the Chama syncline. Superimposed on the Archuleta-Anticlinorium are numerous smaller-scale folds and faults.

Initial Laramide structural development of the Gallina-Archuleta arch began ~78-75 Ma based on the stratigraphic omission of the Pictured Cliffs Sandstone along the southwest limb of the southern part of the anticlinorium (Baltz, 1967). Major uplift, however, did not occur until Paleocene to Eocene time (Cather, 2004). Structural development of the Gallina-Archuleta arch ceased prior to deposition of the volcaniclastic Conejos Formation in the late Eocene-early Oligocene (Brister and Chapin, 1994).

3.4 Gallina Fault

The NNE-SSW-striking Gallina fault is subvertical and alternates from west-down to east-down along its trace (Baltz, 1967; Woodward et al., 1992). At the southern part of the Gallina uplift, the fault is down to the west with a maximum stratigraphic separation of about 490 m where a syncline on the west side is juxtaposed with a poorly defined NW-SE-trending anticline on the east side (Figure 9). At the northern end of the Gallina uplift this fault is called the Tierra Montanosa fault by Woodward et al. (1992), and offsets Pennsylvanian, Permian, Triassic, and Jurassic strata with east side down separation, having a maximum of 550 m of stratigraphic separation. Most researchers interpreted the two faults to connect and called them the Gallina fault (Cather, 2004). The Gallina fault appears to terminate to the north in the area south of El Vado reservoir, where it splays into a closely spaced, polygonal set of small-displacement faults (Landis and Dane, 1967).

Baltz (1967) interpreted the Gallina fault to be a dextral strike-slip fault with small but unspecified displacement. Cather (2004) argued the Gallina fault was subparallel to the interpreted net Laramide relative motion vector between the Colorado Plateau and North American craton, and was in the correct orientation for dextral-slip relative to the dominant NE-SW shortening direction as shown by the orientation of folds in the eastern San Juan basin and in the Gallina-Archuleta arch.

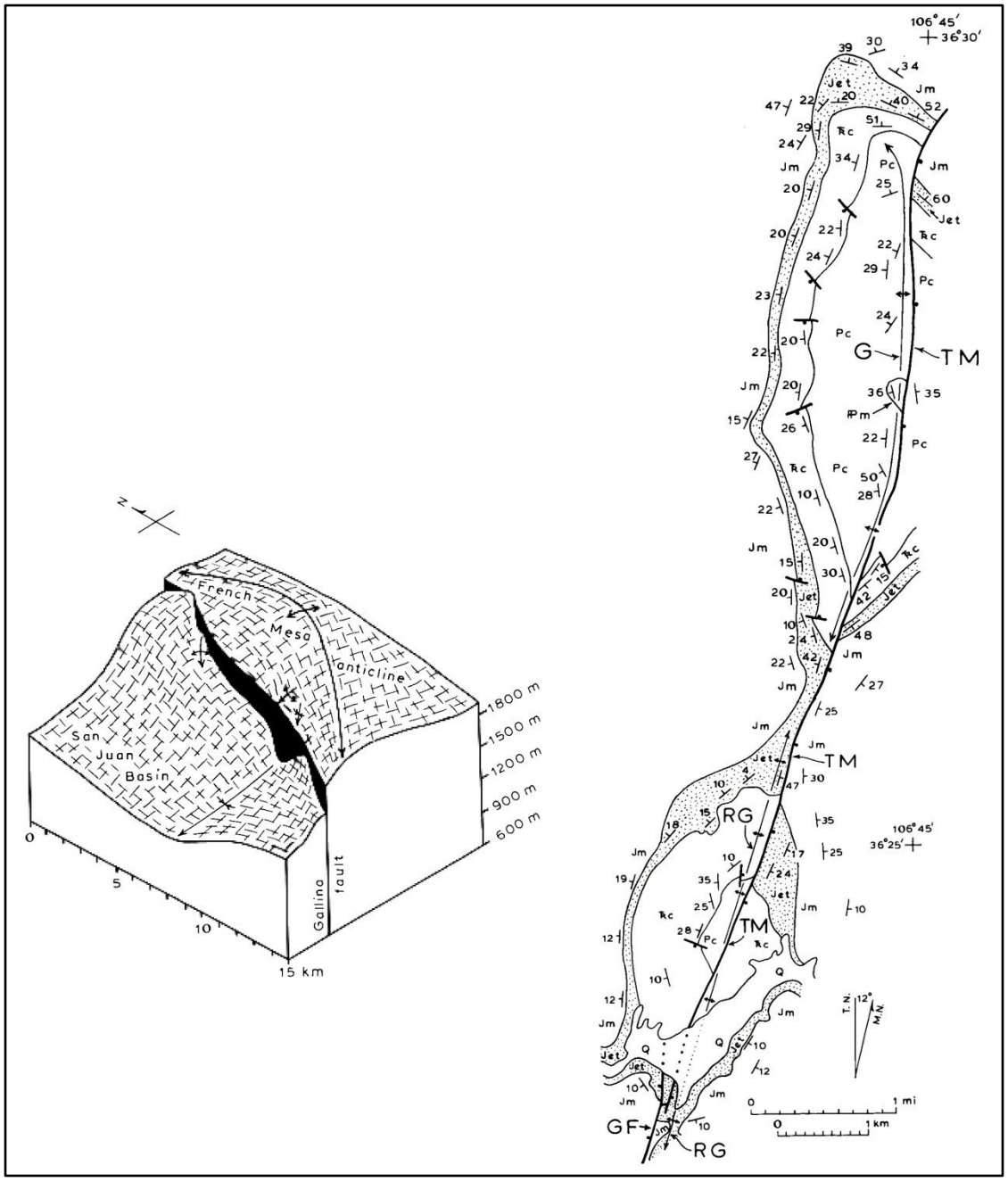

Figure 9. Generalized block diagram and Geological map of the Gallina fault showing configuration of top of Permian strata along the Gallina fault. Elevation is above sea level; Pc, Permian Cutler Formation; Trc, Triassic Chinle Formation; Jet, Jurassic Entrada and Todilto Formation; Jm, Jurassic Morrison Formation; G, Gallina anticline; GF, Gallina fault; TM, Tierra Montanosa fault. Modified from Woodward (1992).

3.5 Stratigraphy

In north-central New Mexico, the Nacimiento uplift exposes Precambrian crystalline basement in its core including mafic dikes, aplite dikes, gneiss, mafic metavolcanic rocks, felsic metavolcanic rocks, and metasedimentray rocks. In the Gallina uplift, the oldest exposed strata are much younger with Paleozoic and Mesozoic strata observed within the uplift (Figure 10). The western margin of the Nacimiento uplift and the Gallina uplift defines the eastern boundary of the San Juan basin which consists of the Paleozoic, Mesozoic, and Cenozoic strata including Culter Formation (Pc), Chinle Formation (Trc), Entrada Sandstone (Je), Todilto Formation (Jt), Morrison Formation (Jm), Dakota Formation (Kd), Mancos Shale (Km), Mesaverde Group (Kmv), Lewis Shale (Kl), Fruitland and Kirtland Formation (Kkf), Ojo Alamo Sandstone (Toa), Nacimiento Formation (Tn), and San Jose Formation (Tsj).

From the Turonian to early Campanian time (~95-80 Ma) north-central New Mexico occupied a portion of the Western Interior basin with subsidence recorded in the Mancos Shale, Point Lookout Sandstone, and Menefee Formation. The thickness of the Mancos Shale in the axial part of the San Juan basin reaches 643m, similar to the thickness near Mesa Verde National Park. This illustrates that differential subsidence had not begun in the San Juan basin prior to ~80 Ma (Cather, 2004).

Initial Laramide deformation in the research area began at ~80-75 Ma, broadly coeval with the beginning of the final marine transgression which is recorded by deposition of the Cliff House Sandstone, Lewis Shale, and Pictured Cliffs Sandstone. Following the northeastward retreat of the Lewis Sea and the regressive Pictured cliffs

shoreline, coal-bearing coastal plain deposits of the Fruitland Formation accumulated in the San Juan basin. The Kirtland Formation transitionally overlies the coal-bearing Fruitland Formation and is deposited in an alluvial plain environment. The Kirtland and Fruitland Formation consist of black, gray shale with interbedded gray to buff, poorly sorted sandstone with a thickness of ~100 m. At the top of the Kirtland Formation a significant unconformity divides the Kirtland Formation from overlying the Ojo Alamo Sandstone (Fassett, 2000). The unconformity occurs 4.9 m above a volcanic ash bed in the upper part of the Kirtland Formation that has been dated at ~73 Ma by the $^{40}Ar/^{39}Ar$ (Fassett and Steiner, 1997). The Ojo Alamo Sandstone is found throughout the research area and consists of sandstone, pebbly sandstone, and conglomerate with a thickness of ~30 m (Sikkink, 1987). The overlying Early to Late Paleocene Nacimiento Formation consists of olive-green and gray, carbonaceous shale with poorly sorted sandstone and is as much as 500 m thick. The Nacimiento Formation is overlain in angular unconformity by the Eocene San Jose Formation. The San Jose Formation represents the final preserved episode of Laramide sedimentary aggradation in the research area and is as much as 550 m thick (Cather, 2004).

In this study my 3D structural model focuses on the Morrison Formation, Dakota Formation, Mancos Shale, Mesaverde Group, and Lewis Shale (Figure 11). These strata are chosen as they are regionally extensive and laterally continuous across the San Juan basin and the Gallina uplift. Further, from the well data and published geologic maps, there is no obvious change on the thickness of these strata. Therefore they make good

strain markers to study Laramide deformation. The description of these units is as follows (Crouse et al., 1992):

Jm- Morrison Formation (Late Jurassic): The Morrison Formation consists of three informal members which are, in ascending order: brownish-maroon siltstone, mudstone, and very fine grained sandstone with light-gray sandstone and red, silicified conglomerate; brick-red and pale-green mudstone and gray to yellow-buff, arkosic sandstone; and white, kaolinitic, conglomeratic sandstone. The total thickness is ~ 200 m.

Kd- Dakota Formation (Late Cretaceous): The Dakota Formation consists of three units which are, in ascending order: tan to brown, well-sorted, fine-grained quartzose sandstone; gray and black shale with interbedded carbonaceous shale, coal, and siltstone; and tan, fine-grained, well-sorted quartzose sandstone. The total thickness is ~50 m.

Km- Mancos Shale (Late Cretaceous): The Mancos Shale is dark-gray and black shale with thin beds of finely crystalline limestone and calcareous sandstone and subordinate septarian and silty limestone concretions. The total thickness is ~650 m.

Kmv- Mesaverde Group (Late Cretaceous): The Mesaverde Group consists of three units which are, in ascending order: tan, fine-grained sandstone with salt and pepper texture; gray and black shale with interbedded carbonaceous shale, coal, ironstone, and sandstone; and tan, medium-grained sandstone. The total thickness is ~200 m.

Kls- Lewis Shale (Late Cretaceous): The Lewis Shale consists of gray, brown, and black shale with minor, thin siltstone, fine-grained sandstone, finely crystalline limestone, and fossiliferous limestone interbeds. The total thickness is ~500 m.

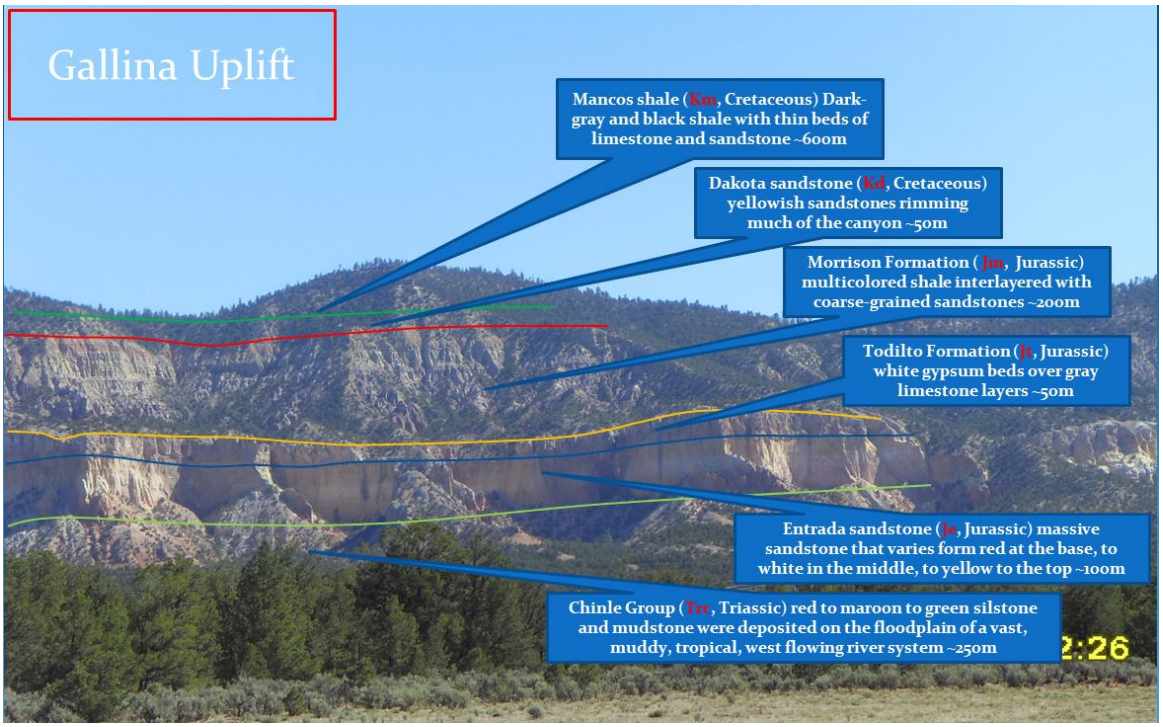

Figure 10. Exposed strata in the Gallina uplift including the Chinle Formation, Entrada Sandstone, Todilto Formation, Morrison Formation, Dakota Formation, and Mancos shale. Units description from Crouse et al. (1992).

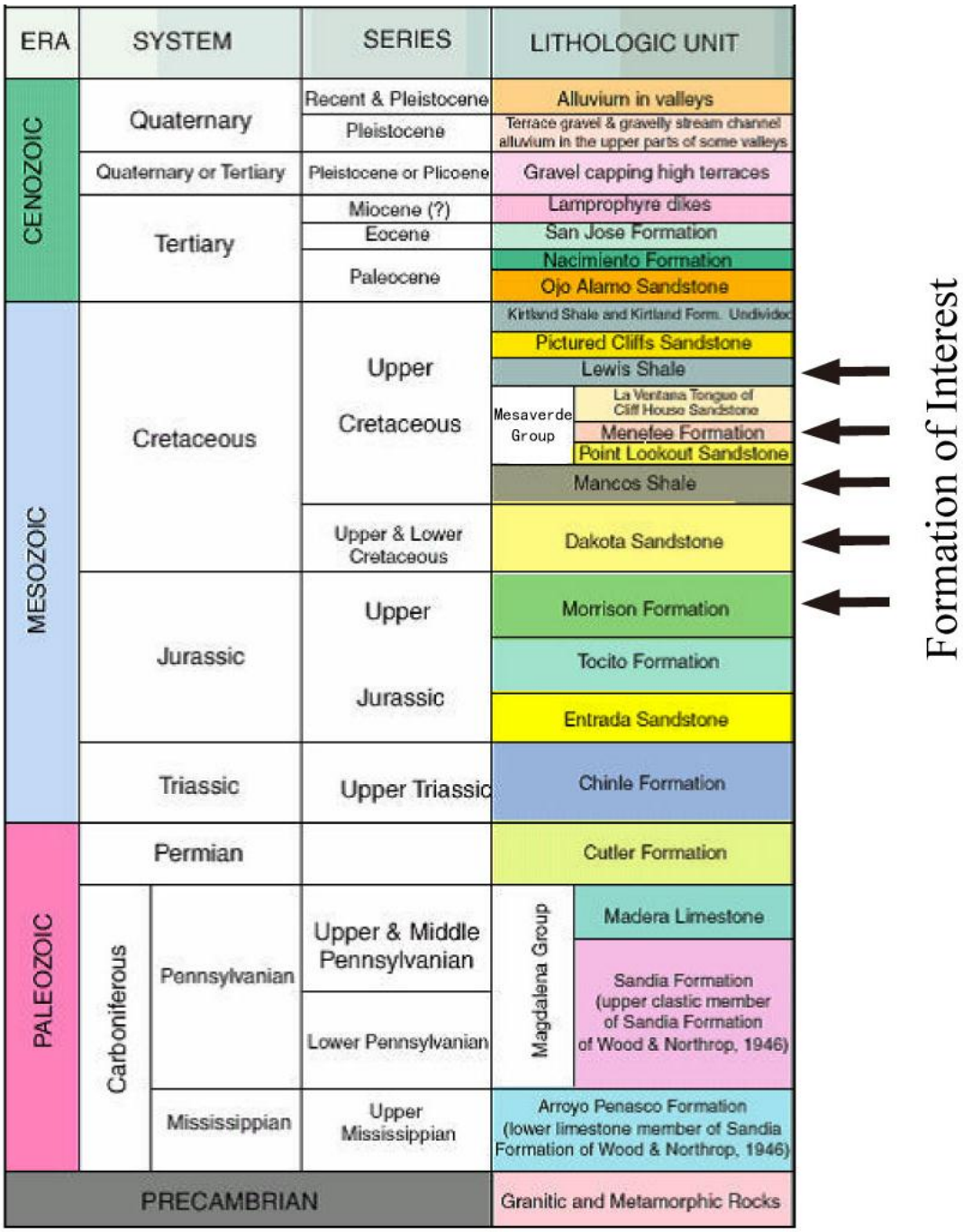

Figure 11. Stratigraphic chart showing formations of interest including the Morrison Formation, Dakota Formation, Mancos Shale, Mesaverde Group, and Lewis Shale. Modified from Reeves and Billingsley (2002).

4. Regional Structure Surface Modeling

4.1 IDW Interpolation

In the San Juan basin, obtained well data includes the elevation information of different formation contacts. This research focuses on several stratigraphic horizons which predate the main Laramide movement in the area of the Nacimiento uplift and the Gallina uplift, and are interpreted to have been of relatively uniform thickness across the region prior to the orogeny. These formation contacts include the top of the Morrison Formation, the Dakota Formation, the Mancos Shale, the Mesaverde Group, and the Lewis Shale. Along the boundary between the San Juan Basin and the Nacimiento and Gallina uplifts, points for the elevation of formation contacts are extracted from geologic maps draped over a DEM.

These points are interpolated into a surface based on Inverse Distance Weighted (IDW) with the software ArcGis. IDW interpolation explicitly implements the assumption that things that are close to one another are more alike than those that are farther apart. To predict a value for any unmeasured location, IDW uses the measured values surrounding the prediction location. The measured values closest to the prediction location have more influence on the predicted value than those farther away. A surface calculated using IDW depends on the selection of the power value and the search neighborhood strategy. In this research the power used is 2 and the search radius is nearby 12 points. IDW is an exact interpolator, where the maximum and minimum values in the interpolated surface can only occur at sample points.

4.2 3D Structural Surfaces

To interpolate each surface across the research area, the well data and contact line points from the Morrison Formation, Dakota Formation, Mancos Shale, Mesaverde Group, and Lewis Shale are interpolated together based on the assumption that the formation thicknesses are constant. The thicknesses used are: 50 m for the Dakota Formation, 650 m for the Mancos Shale, 200 m for the Mesaverde Group, and 500m for the Lewis Shale. Based on the above assumptions, the different stratigraphic surfaces are interpolated in ArcGIS (Figure 12). These surfaces cover the area of the San Juan basin, the Gallina uplift, and the Chama basin. In the Nacimiento uplift where Precambrian basement is exposed, the high-angle Nacimiento fault is set as the boundary of these surfaces. These surfaces are then transferred into the software Move to make 3D structural surfaces (Figure 13).

From these surfaces, several interesting structural observations can be made. The San Juan basin is an asymmetric syncline with an axis which trends NW. This feature is consistent with observations by earlier researchers (Baltz, 1967; Woodward, 1974; Cather, 2004). The eastern boundary of the San Juan basin is marked by a monocline along the west side of the Gallina-Archuleta arch and the Nacimiento uplift. On the western margin of the Nacimiento uplift, the Nacimiento fault breaches the surface. At the northern end of the Nacimiento uplift the exposed N-S-striking high-angle Nacimiento reverse fault disappears at the surface. To the north, another monocline forms directly along strike of the Nacimineto fault to the east of the westernmost monocline which forms the boundary of the Gallina uplift. Further to the north within the Gallina uplift a third monocline

branches off the one described above and several small anticlines develop on the Gallina-Archuleta arch between the monoclines as their axial traces spread out. These structural features are consistent with descriptions and published structural maps (Figure 14) from earlier researchers (Baltz, 1967; Woodward, 1974; Crouse et al., 1992; Cather, 2004; Pollock et al., 2004). Based on comparisons with published regional geologic maps, the 3D model does a good job reflecting the observed structures in the research area. One key observation is that along the western boundary of the San Juan basin, the western monocline can be observed to extend continuously from the Nacimiento uplift to the Gallina uplift (Figure 13).

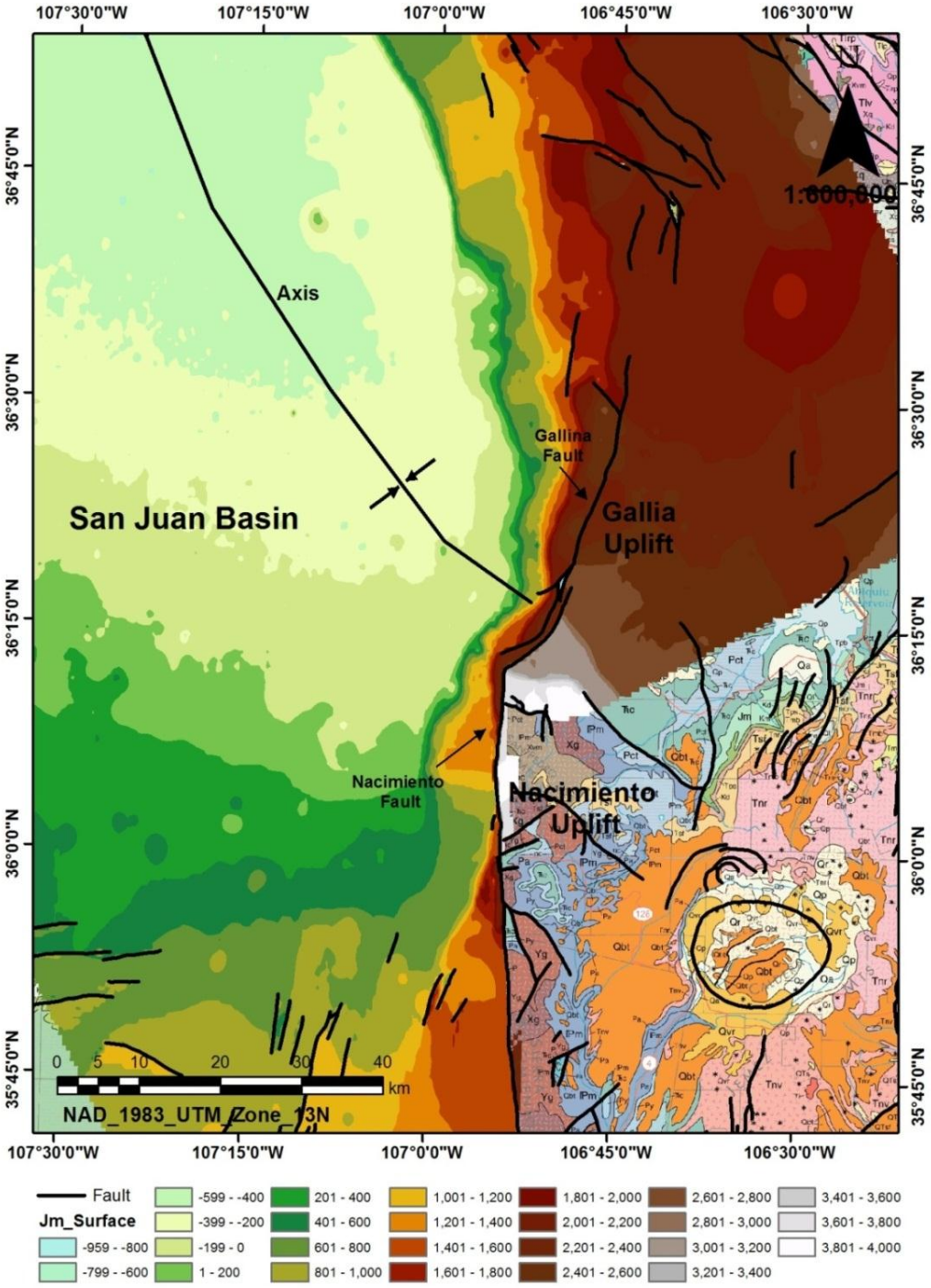

Figure 12. The surface of the Morrison Formation in ArcGis overlaying on the regional geologic map, showing the Nacimiento uplift, Gallina uplift, San Juan basin, Nacimiento fault, Gallina fault, and the location of the San Juan basin axis.

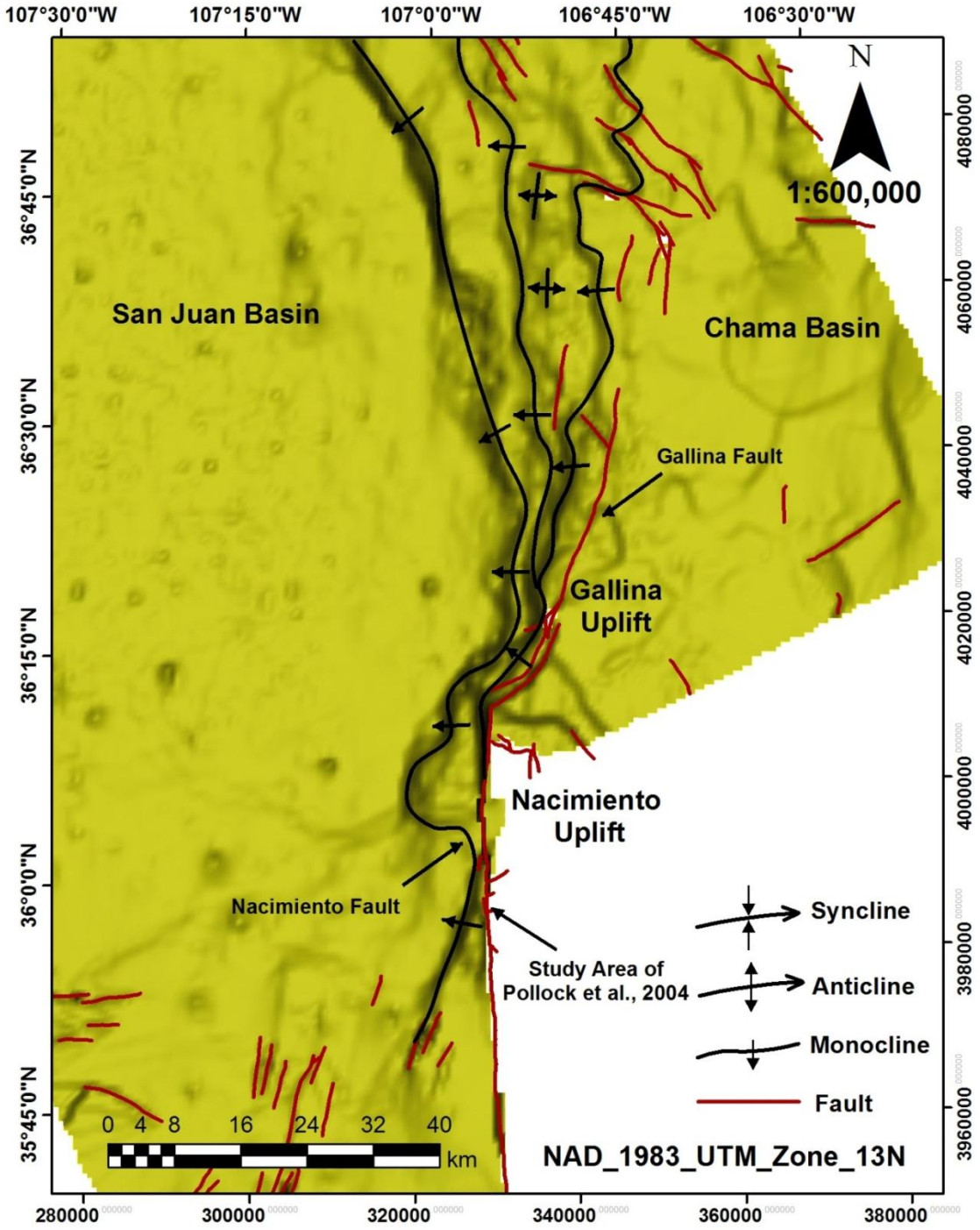

Figure 13. Structural surface of the Mancos Shale in Move showing the location of the cross section from Pollock et al. (2004) and the structures on the surfaces including the western monocline, eastern monocline, anticlines, Nacimiento fault, and Gallina fault.

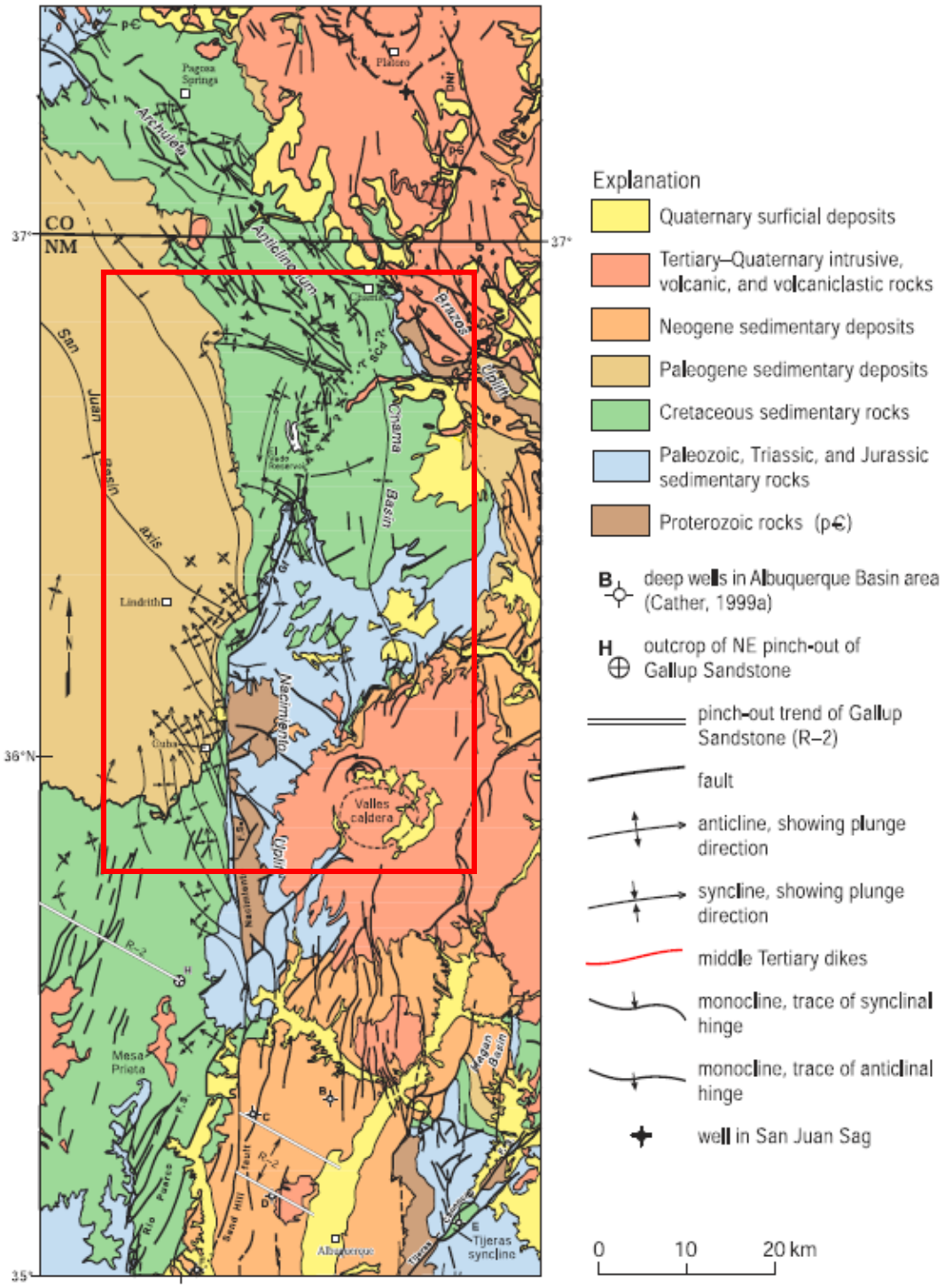

Figure 14. Simplified geologic map of the eastern San Juan basin, Nacimiento uplift, and Gallina-Archuleta arch, the area of 3D structural surface in the red box. **Gf**, Gallina fault; **SCd**, Salado-Cumbres discontinuity; **DNf**, Del Norte fault. Modified from Cather (2004).

4.3 Cross Sections

As described above, a key observation is that at the northern end of the Nacimiento uplift, the Nacimiento fault disappears beneath outcrops of Jurassic strata while along the projected trace of the Nacimiento fault to the north, another monocline forms and extends along the Gallina-Archuleta arch (Figure 13). I interpret this relationship to indicate that the Nacimiento fault changes from a breakout fault along the Nacimiento uplift to a blind fault under the Gallina-Archuleta arch. To address the possible angle of these blind faults and the subsurface geometry of responsible structures under the Gallina-Archuleta arch, I make 5 E-W-oriented cross sections from the northern end of the Nacimiento uplift to the Gallina-Archuleta arch. These include a cross section across the northern end of the Nacimiento uplift, 3 cross sections across the Gallina uplift, and a cross section on the northern Gallina-Archuleta arch (Figure 15, 16, 17, 18, 19, and 20). These cross sections focus on the structural geometry of the western boundary of the Nacimiento and Gallina uplifts.

In cross section 1 (Figure 16), structures consist of two monoclines; a western monocline and a structurally higher eastern monocline. Structural relief between these two monoclines is ~2.8 km and between the western monocline and the San Juan basin is ~1.2 km for a total of ~4.0 km of structural relief. This cross section is across the northern end of the Nacimiento uplift where the high-angle Nacimiento reverse fault is observed in outcrops of Jurassic strata. In cross section 2 (Figure 17), structural relief between these two monoclines decreases to ~2.0 km as the Nacimiento fault becomes blind. There is almost no change in structural relief between the western monocline and

the San Juan basin which yields a total of ~3.2 km of structural relief. On the eastern monocline two high-angle faults (Gallina fault and Canada fault) are down to the west with ~0.3 km and ~0.2 km displacement. In cross section 3 (Figure 18), structural relief between the western monocline and the eastern monocline is ~1.8 km. Structural relief between the western monocline and the San Juan basin changes little and yields a total of ~3.0 km of structural relief. The Gallina fault develops on the eastern monocline with only ~0.1 km of displacement. Cross section 4 (Figure 19) shows a third lower monocline between the western and eastern monoclines. Structural relief between the western monocline and the lower monocline is ~0.8 km and between the lower monocline and the eastern monocline is ~1.0 km. The total structural relief across the three monoclines is ~3.0 km. The Gallina fault on the eastern monocline changes to east-down with ~0.2 km displacement. Cross section 5 (Figure 20) is across the northern Gallina-Archuleta arch and shows two smaller monoclines between the western monocline and the eastern monocline. The total structural relief across all structures is ~3.2 km. In general, the western monocline extends from the northern end of the Nacimiento uplift to the Gallina-Archuleta arch and the monocline geometry on these cross sections appears similar. The vertical relief of the western monocline is ~1.2 km and the relief changes little from the Nacimiento uplift to the Gallina-Archuleta arch.

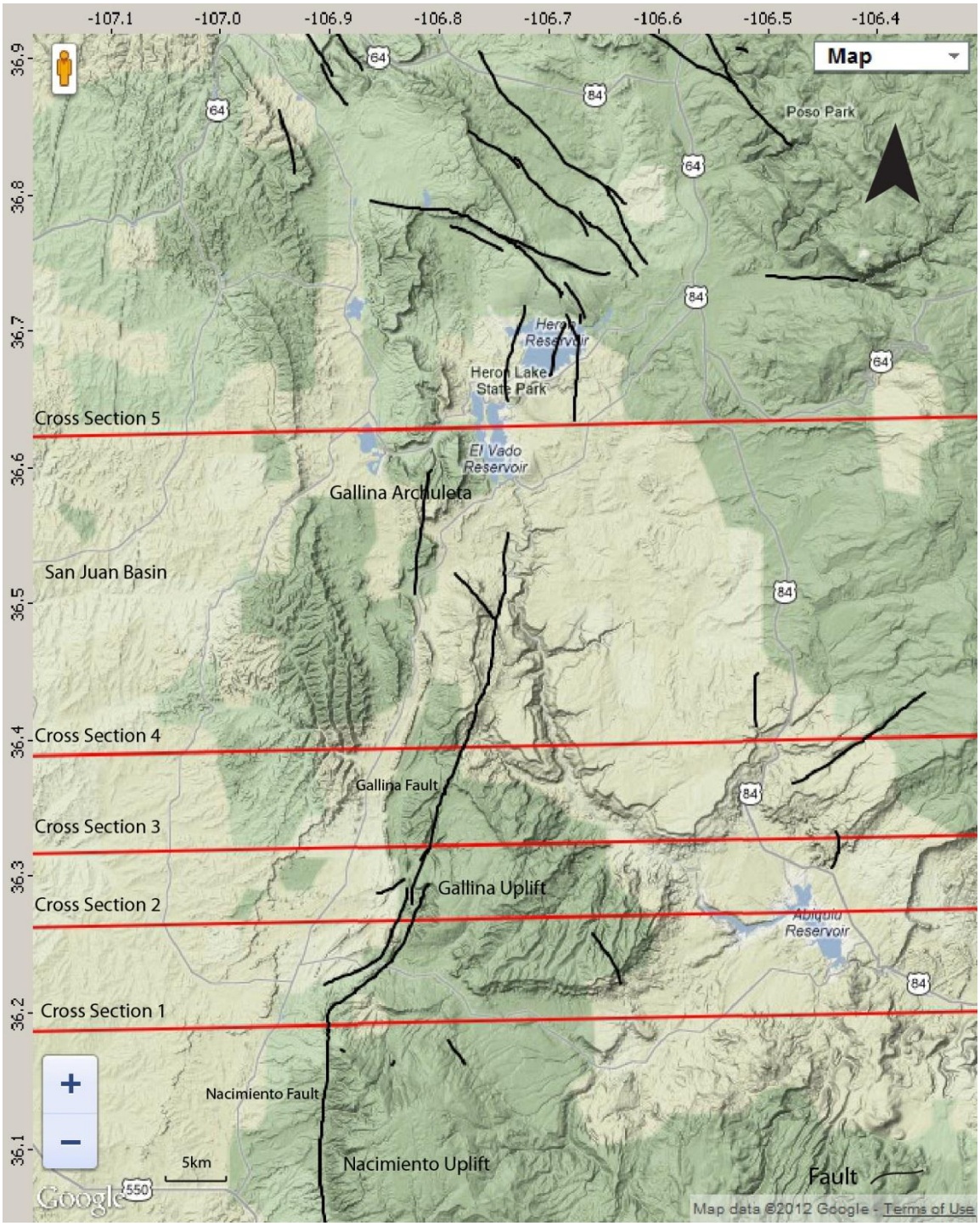

Figure 15. Google map showing the locations of 5 cross sections from the northern end of the Nacimiento uplift to the Gallina-Archuleta arch.

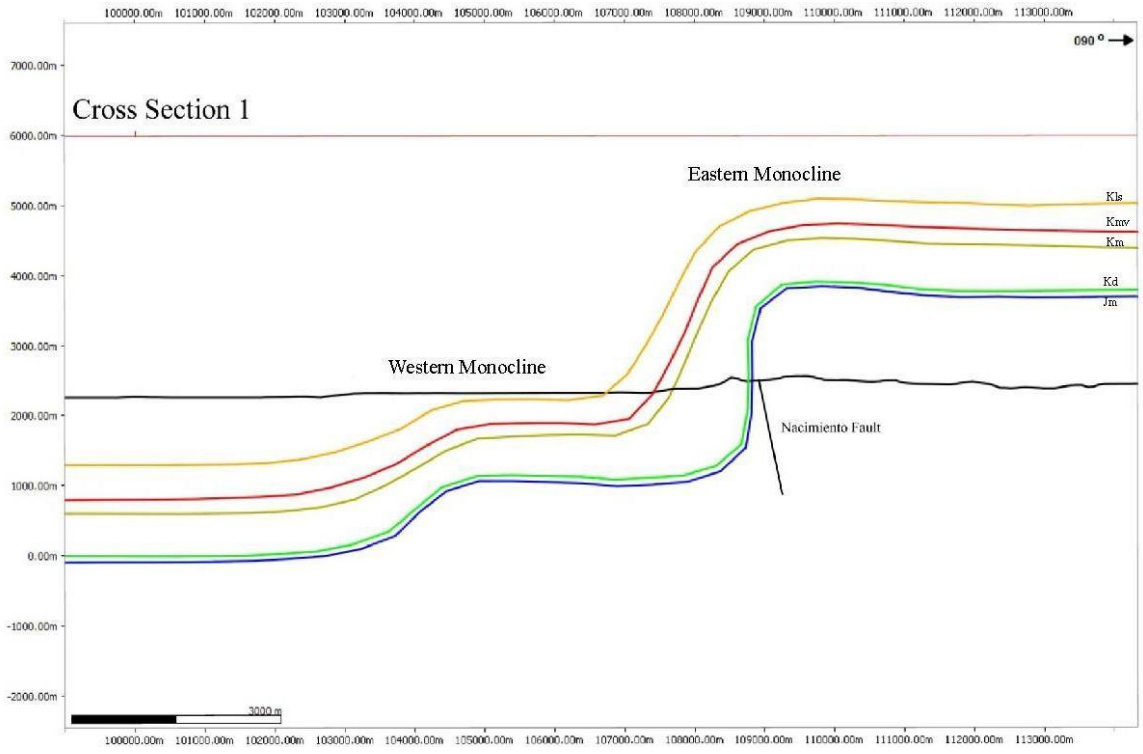

Figure 16. Cross section 1 at the northern end of the Nacimiento uplift showing the western monocline, eastern monocline, and Nacimiento fault breakout location.

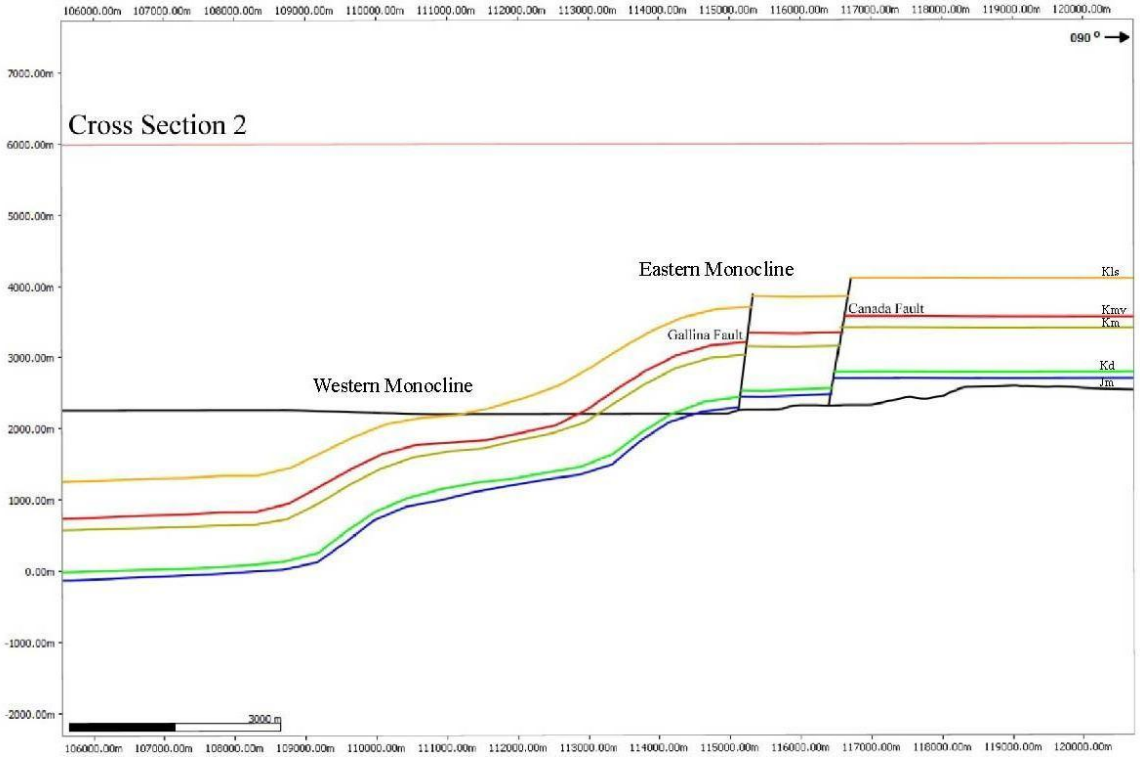

Figure 17. Cross section 2 across the Gallina uplift showing the western monocline, eastern monocline, Gallina fault, and Canada fault.

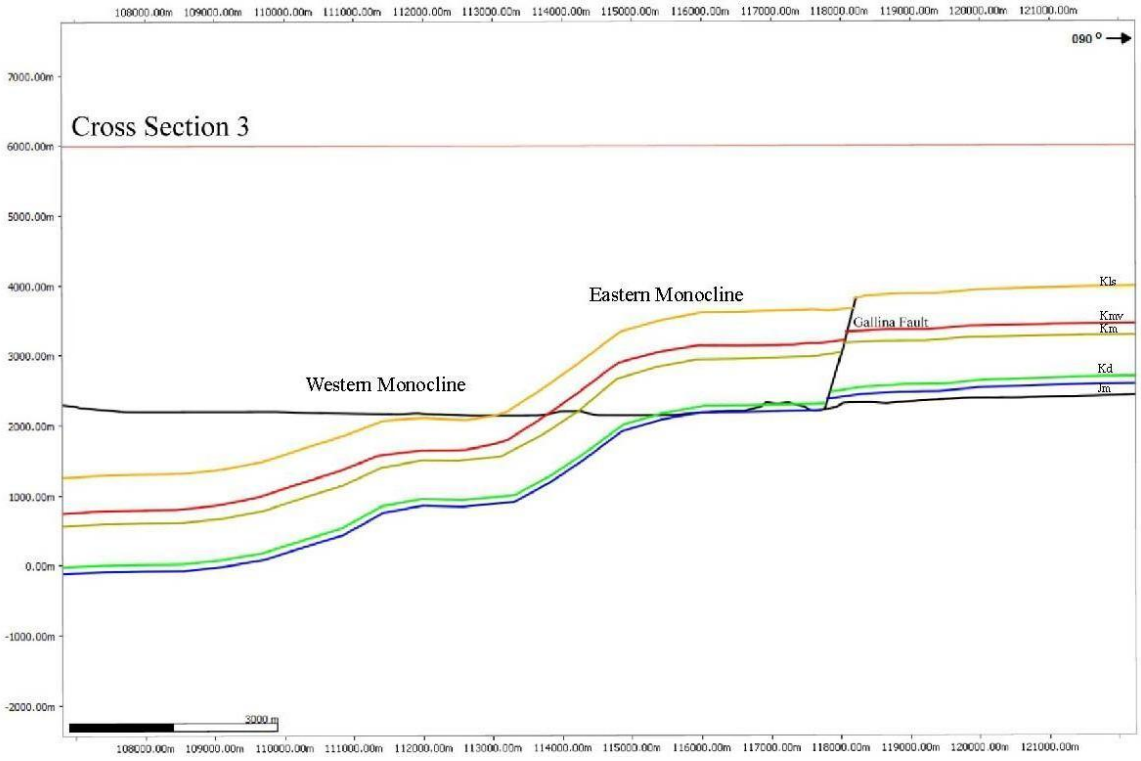

Figure 18. Cross section 3 across the Gallina uplift showing the western monocline, eastern monocline, and Gallina fault.

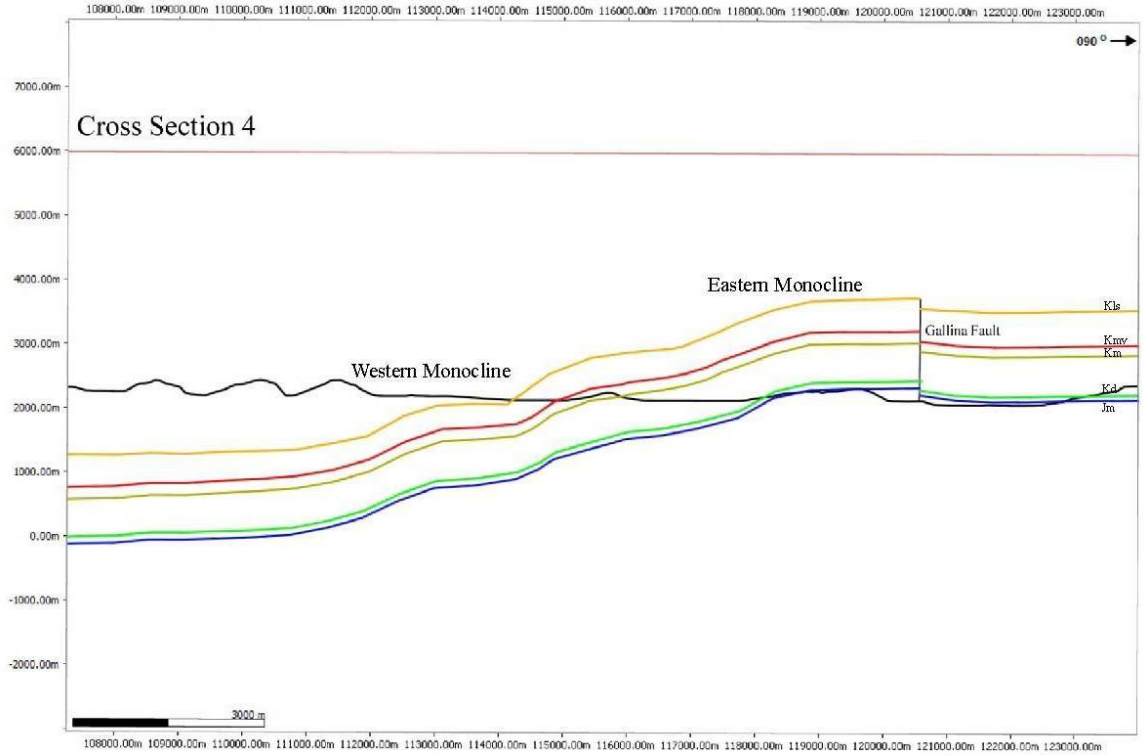

Figure 19. Cross section 4 across the Gallina uplift showing the western monocline, eastern monocline, and a smaller monocline between them.

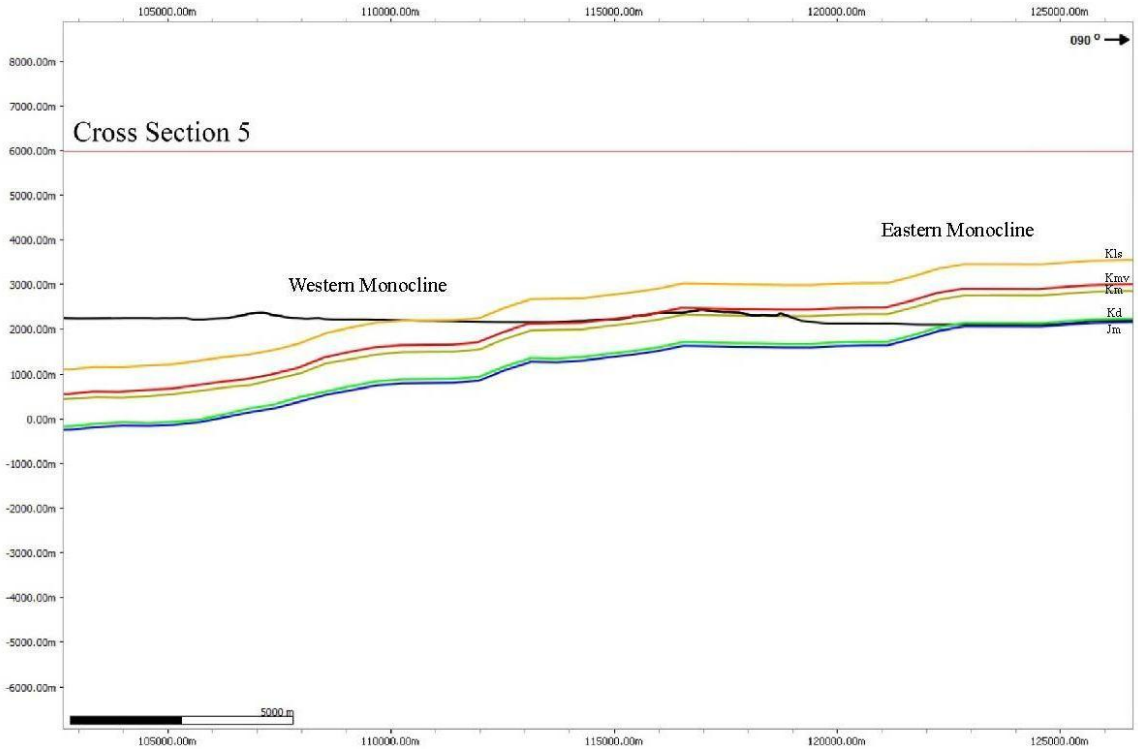

Figure 20. Cross section 5 across the Gallina-Archuleta arch showing the western monocline, eastern monocline, and two smaller monoclines between them.

5. Trishear Model and E-W Shortening

5.1 Introduction

Fault-propagation folds are a common folding mechanism in fold and thrust belts which occur when a propagating thrust fault loses slip and terminates upsection by transferring its shortening to a fold developed at its tip (Mitra, 1990). Structures characterized by this general relationship have been recognized and interpreted in a number of fold and thrust belts. Suppe and Medwedeff (1990) used kink-band migration to explain the relationships between fault tips, displacement and fold geometry. However, the kink-band model predicts uniform bed dips and homogeneous deformation in fold limbs and is not suited for basement-cored anticlines, fold-fault geometries with footwall synclines, structures with deformation-induced variable limb thickness, and folds with progressive rotation of the forelimbs (Allmendinger, 2000).

Erslev (1991) put forward an alternative trishear kinematic model for fault propagation folds which holds that the strong brittle deformation of the underlying fault is accommodated by a triangular-like widening-upward distributional shear zone, with the triangle apex pinned to the fault tip. Hardy and Ford (1997) expanded Erslev's (1991) initial trishear model by presenting a mathematical formulation of the problem (Figure 21). In this formulation the magnitude of slip decreases from Vo at the boundary of trishear zone in the hanging wall to zero at the boundary of the trishear zone in the footwall and the direction of slip is varied from parallel to the fault dip at the top of the trishear zone to parallel to the base of the zone at the lower boundary of the zone. The trishear algorithm can be utilized for forward modeling fault-related folds.

Allmendinger (1998) further discussed the influence of six trishear parameters including 1) fault ramp angle, 2) fault slip, 3) and 4) X and Y positions of the tip line, 5) trishear apical angle, and 6) P/S (propagation to slip) ratio. The P/S ratio defines the rate of the propagation of the fault tip line in the direction of slip, relative to the rate of slip of the hanging wall and controls the distance that the tip line of the fault has propagated from its initial crack. The P/S ratio exerts the most important control on the amount of strain in a trishear structure with the lower the P/S ratio, the more ductile the behavior of the deformed beds.

Allmendinger et al. (2004) discussed three modes of fault nucleation and propagation including 1) propagation of the tip line from a subhorizontal decollement which results in a bent backlimb; 2) propagation from the tip of the old fracture for the case of reactivation; and 3) symmetric propagation from an initial flaw within the crust (Figure 22). According to Yin and Ingersoll's (1997) model, Laramide thrust faults were interpreted to nucleate on a decollement horizon in the middle crust such that the resulting fold should have a fault-bend backlimb. Unfortunately, the late Cenozoic Jemez volcanic field developed on the eastern side of the Nacimiento uplift and the volcanic activity has concealed where the predicted backlimb would be.

As discussed above, along the eastern boundary of the San Juan basin the overturned beds observed by Merrick and Woodward (1982), the thickening and thinning of beds observed by Pollock et al. (2004), and the basement cored uplifts indicate the trishear kinematic model is the most appropriate method to model and interpret these structures. This study uses Move to forward model the formation of the Gallina uplift.

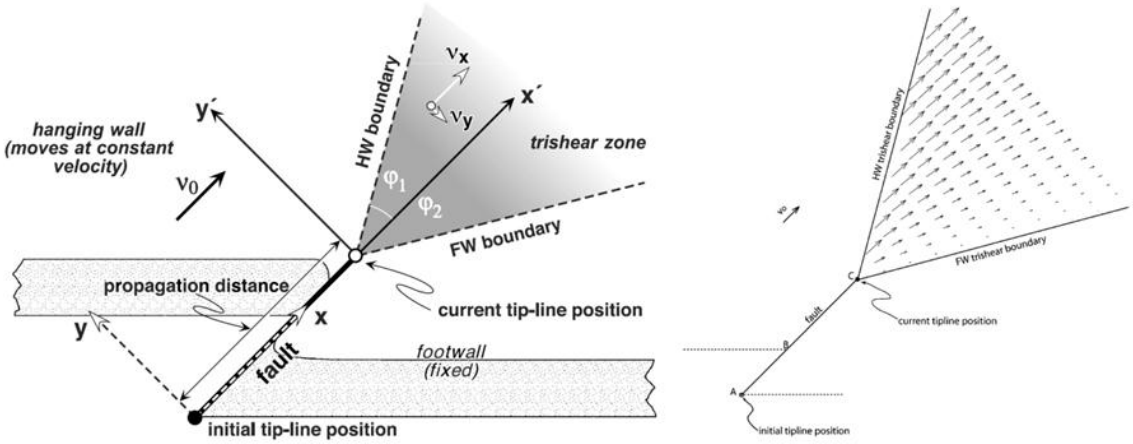

Figure 21. The velocity-based description of the trishear kinematics first presented by Hardy and Ford (1997).

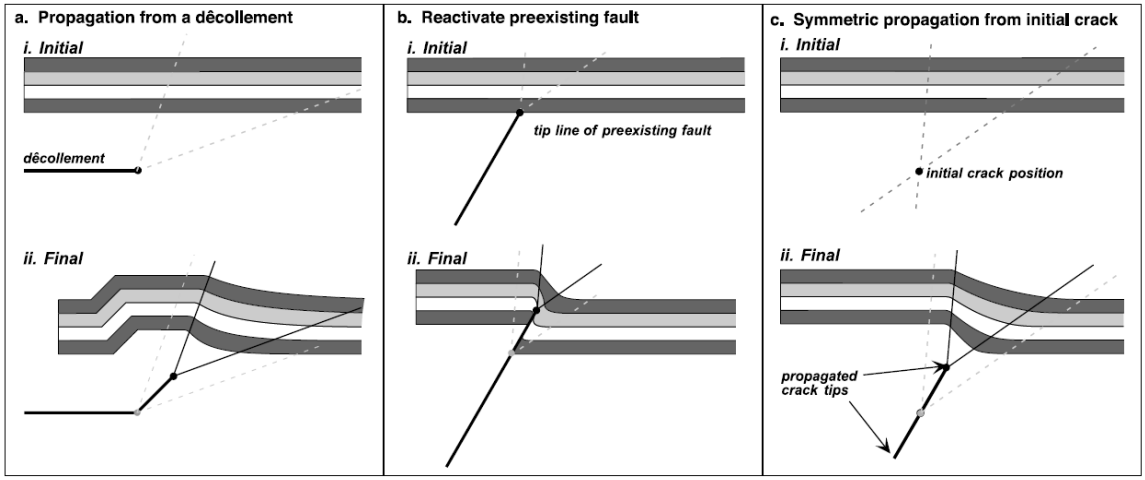

Figure 22. Three modes of fault nucleation and propagation. Modeling the fold shape yields slip and propagation, allowing one to determine objectively which mode is responsible. (a) Propagation of the tip line from a decollement; (b) propagation from the tip of the old fracture for the case of reactivation; (c) symmetric propagation from an initial flaw within the crust, with displacement diminishing downward as well as upward in mirror-symmetry trishear zones (Allmendinger et al., 2004).

5.2 Forward Models

In this study, I generated a series of forward trishear fold models and compared them with the monocline geometry in the cross sections to find the best fit trishear parameters. In regard to the six parameters defined by Allmendinger (1998), the dip angle of the faults responsible for the formation of the western and eastern monoclines is one of the primary goals. In the initial forward modeling, I varied the dip angle from 15 ° to 85 ° by 5 ° increments generating 15 sets of forward models. In each set, for a fixed angle, the slip distance can be calculated because the structural relief is known from the cross sections. For example, for a fault angle of 30 ° and structural relief of 2.8 km, the slip distance along the fault plane is 5.6 km (2.8 km/sin30 °). A default trishear apical angle of 50 ° is prescribed by the software Move. In each set with the fixed fault dip angle, I varied the P/S ratio by increments of 1.0 from 1.0 to 4.0 (Figure 23) and compared forward models with the monocline geometry in order to determine the first order range of P/S ratio. I subsequently narrowed the change by increments of 0.1 from 1.6 to 2.4 (Figure 24). By comparing the cross section monocline geometry with series of the forward models, I found a P/S ratio of ~2.0 best fits the Laramide fault-propagation folds in north-central New Mexico.

However, as Allmendinger (1998) indicated, the trishear model is complex and six parameters control the geometry of a trishear fold. What's more, in variable trishear deformation, various parameters can change at any time during the evolution of a fault propagation fold. Thus the P/S ratio or the apical angle of the triangular zone can be varied during growth of the structures, or a ramp angle may change during the fault

propagating. Therefore this study has several limitations and is based on several assumptions. First, the geometry of the western monocline on the cross sections was produced from the interpolation of well data and no seismic data is available. This introduced uncertainties in the geometry of the monoclines. Second, the P/S ratio and ramp angle probably changed as the faults propagated through different strata while this research assumed the P/S ratio and the ramp angle fixed. Third, a default trishear angle of 50 °was used in all forward models.

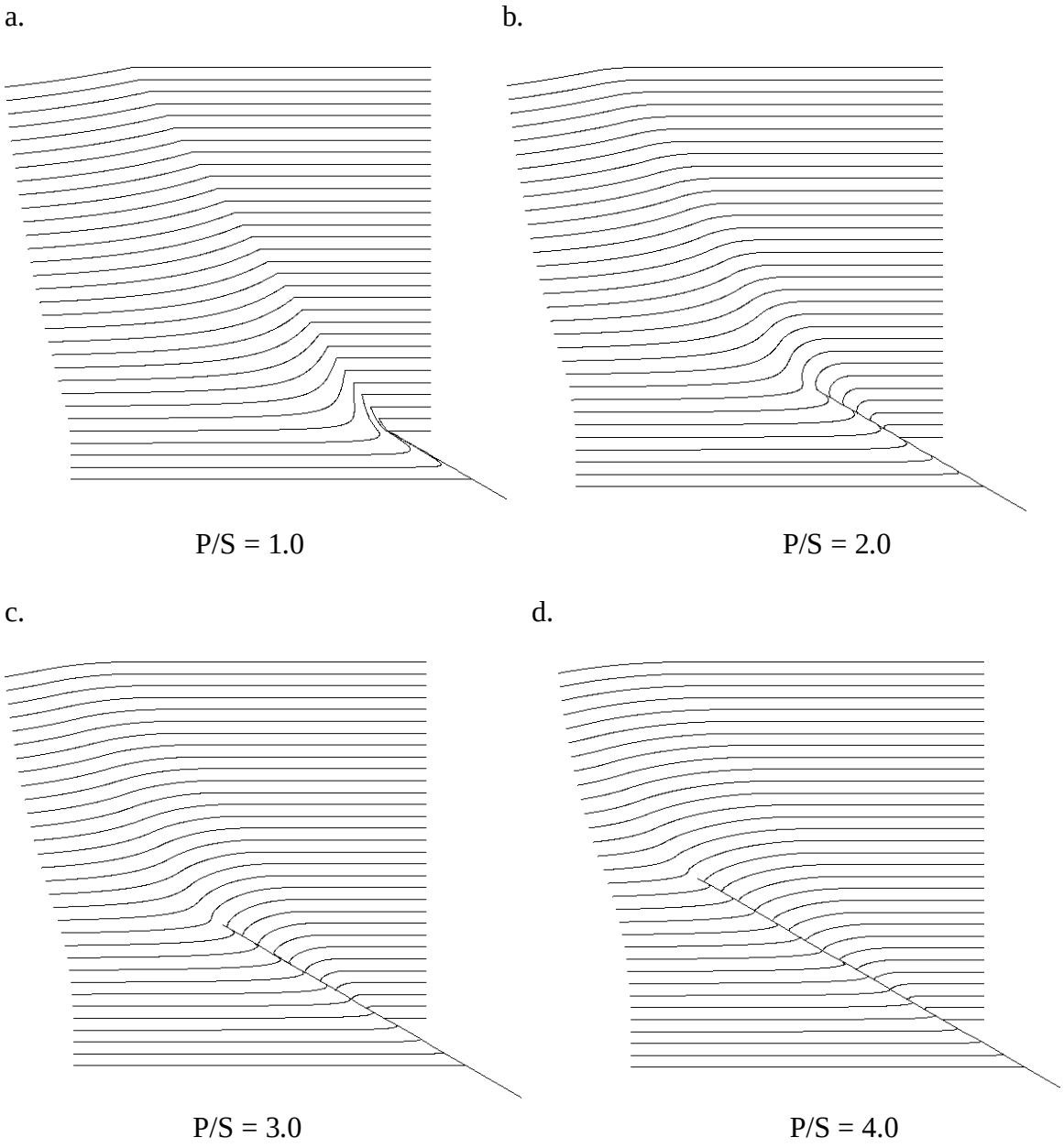

Figure 23. Forward models showing the geometry with ramp angle of 30 ° and slip distance of 5.6 km, a. P/S=1.0; b. P/S=2.0; c. P/S=3.0; d. P/S=4.0.

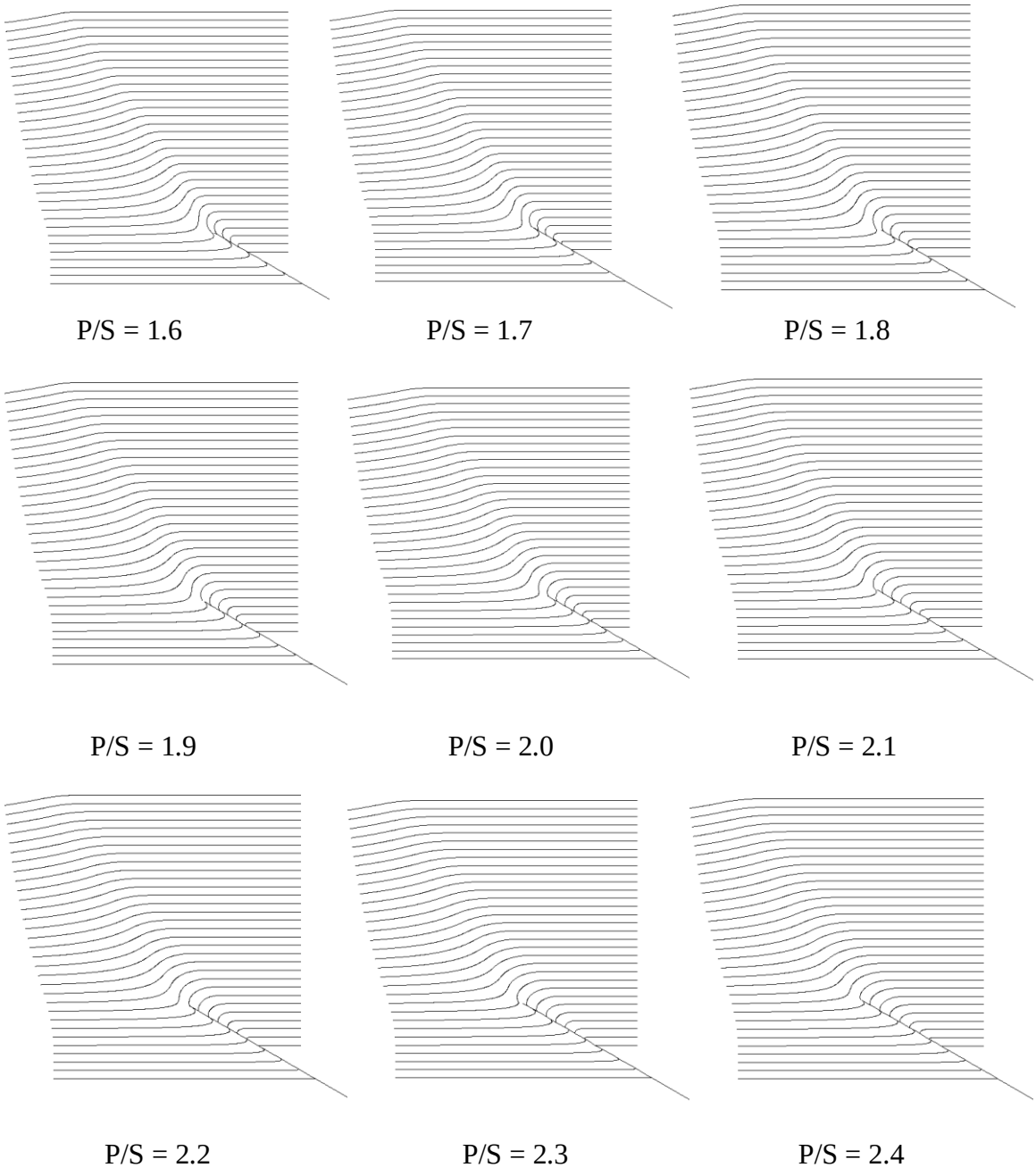

Figure 24. Forward models showing the geometry with ramp angle of 30°, slip distance of 5.6 km, and P/S ratio narrowing from 1.6 to 2.4 by 0.1 increments.

5.3 Forward Modeling of the Western and Eastern Monoclines

The geometry of the western monocline in all 5 cross sections is similar with a structure relief of ~1.2 km. For a fixed ramp angle α, the slip magnitude is 1.2/sinα km based on the structural relief of ~1.2 km. I input these trishear parameters (ramp angle and slip distance) to Move and then varied the P/S ratio by 0.1 increments. By comparing the fold geometries produced from each model with the western monocline on my cross sections, I found the best fit trishear model for the western monocline used a P/S ratio of ~2.0, a fault angle of ~25°, and a slip distance of ~2.8 km (Figure 25). This result is consistent with the interpreted low-angle master fault based on field mapping and gravity data from Pollock et al. (2004).

At the northern end of the Nacimiento uplift, the Nacimiento fault disappears beneath outcrops of Jurassic strata. Along the northward projection of the fault trace into the Gallina uplift, a second monocline overlies the western monocline. I interpret this relationship to indicate that the Nacimiento fault become blind under the Gallina uplift. To the south, Pollock et al. (2004) interpreted the high-angle Nacimiento fault to root into a low-angle master fault. To test the interpretation I modeled the formation of the eastern monocline (Figure 26 and 27). At the northern end of the Nacimiento uplift, the best fit trishear model for the exposed Nacimiento fault has a dip angle of ~70°. Further, my modeling indicates the initial fault tip is located along the low-angle fault (Figure 26). This result is consistent with previous field observations that the Nacimiento fault is a high-angle reverse fault (Baltz, 1967; Merrick and Woodward, 1982; Pollock et al., 2004).

This result supports the interpretation that the high-angle Nacimiento fault may root into the low-angle master fault by Pollock et al. (2004).

To the north within the Gallina uplift, my forward modeling indicates the eastern monocline results from a high-angle blind reverse fault with the initial fault tip also located on the low-angle master fault (Figure 27). Overall, my results supports the interpretation of Pollock et al. (2004) that the Nacimiento uplift is primarily the result of horizontal shortening and developed above a low-angle blind thrust fault, and that the exposed high-angle reverse fault soles downward into the low-angle thrust fault. Further, my regional surface model and kinematic forward models of the Gallina uplift indicate these faults both extend to north, becoming blind beneath the Gallina-Archuleta arch.

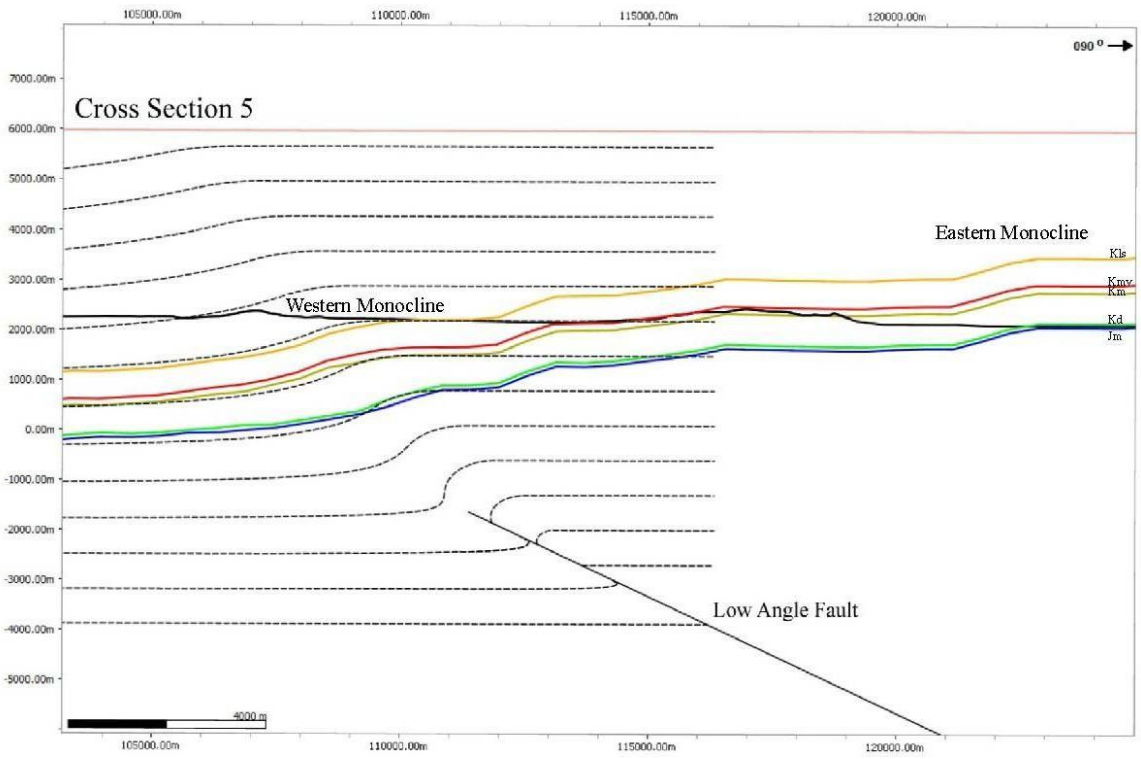

Figure 25. Cross Section 5 overlying by the best fit trishear model (dashed line) with P/S=2.0, fault angle=25 °, and slip=2.8 km showing a low-angle fault responsible for the western monocline.

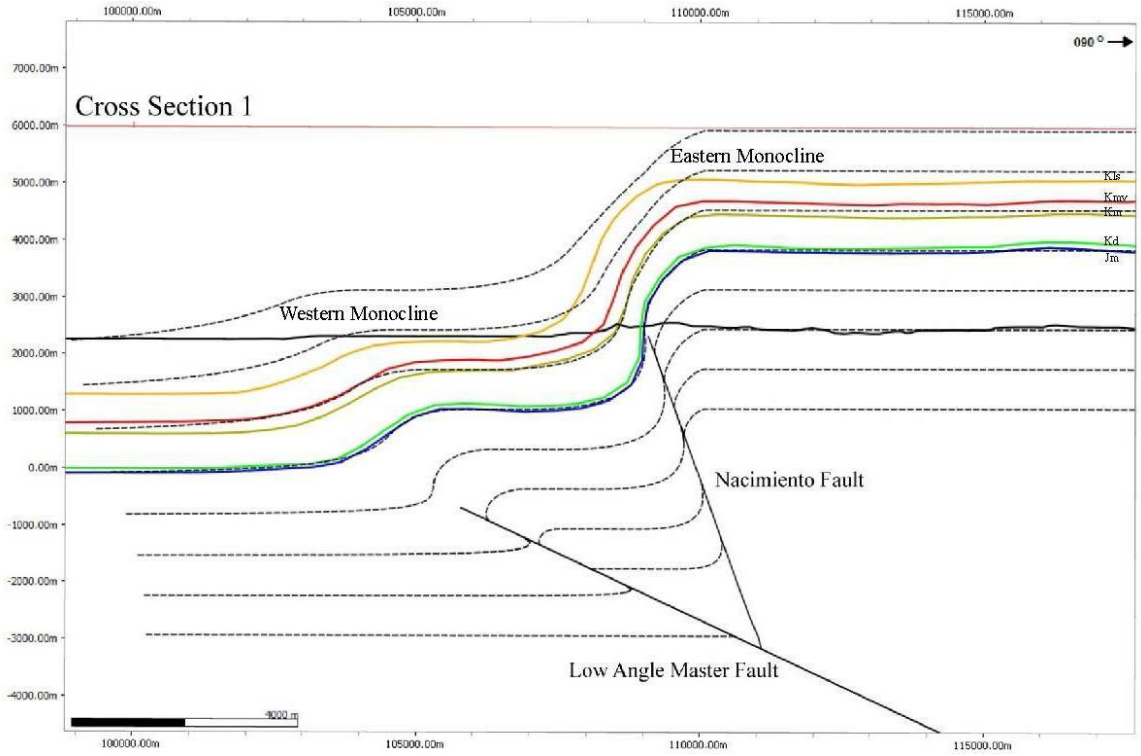

Figure 26. Cross section 1 overlying by the forward model (dashed line) which simulating the formation of the western and eastern monoclines showing the subsurface geometry of the northern end of the Nacimiento uplift.

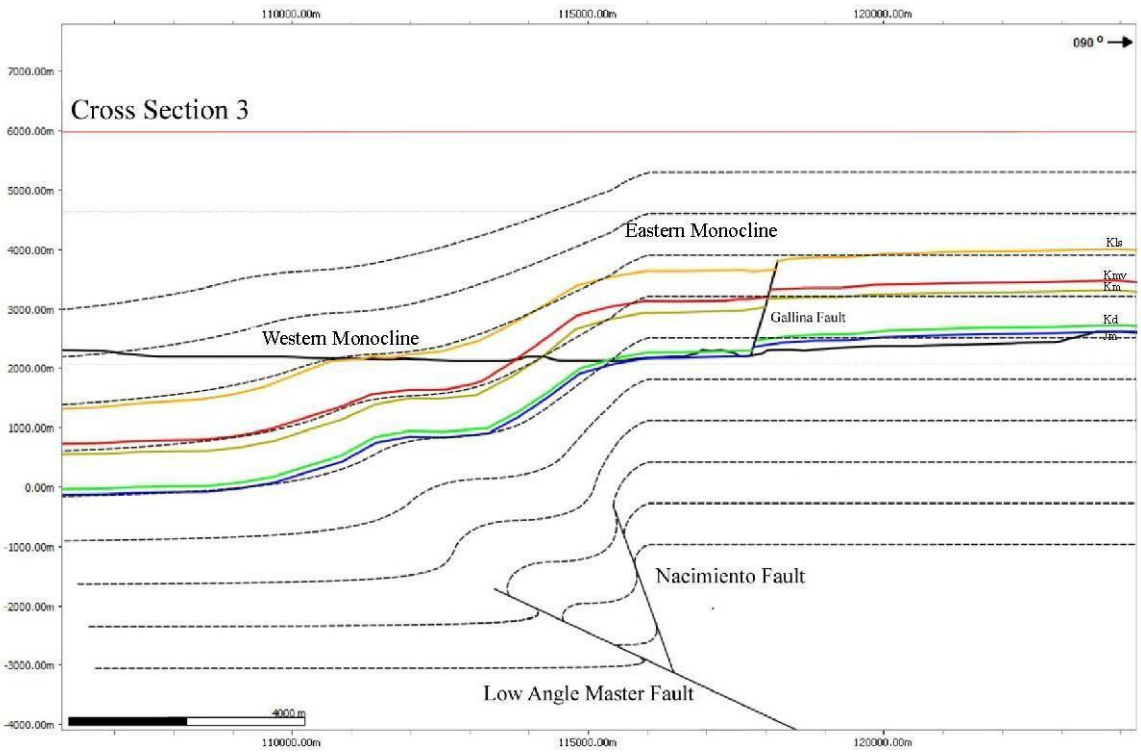

Figure 27. Cross section 3 overlying by the forward model (dashed line) which simulating the formation of the western and eastern monoclines showing the subsurface geometry of the Gallina uplift.

5.4 E-W Shortening on the Cross Sections

In this study, my 3D structural map shows the western monocline extends along the Nacimiento-Gallina uplifts with a total vertical relief of ~1.2 km which is very consistent along its trace. In modeling the formation of the monocline as the result of fault propagation folding, the results indicate the western monocline results from a low-angle thrust fault with a dip angle of ~25°. The calculated E-W shortening along the entire trace of this monocline is ~2.6 km (1.2 km/tan25°).

On cross section 1 (Figure 26) the throw on the exposed Nacimiento fault is ~2.8 km with fault angle of ~70°. The E-W shortening of the eastern monocline should be ~1.0 km (2.8 km/tan70°) but the Nacimiento fault roots into the low-angle master fault. Therefore the fault starts to slip from a 25° fault plane and then the fault dip angle changes to ~70°. Based on this interpretation the real E-W shortening related to the eastern monocline is ~2.7 km (2.8 km/sin70°*cos25°). This results in a total E-W shortening of ~5.3 km at the northern end of the Nacimiento uplift. On cross section 3 the structural relief of the eastern monocline decreases to ~1.8 km where the Nacimiento fault becomes blind beneath the Gallina uplift. By modeling the eastern monocline (Figure 27) as a blind high-angle (~70°) fault which branches from a low-angle (~25°) thrust fault, I obtain a E-W shortening of ~1.7 km (1.8 km/ sin70°*cos25°). This results in a total shortening of ~4.3 km across the Gallina uplift. On other cross sections (Figure 17, 19, and 20) there is no obvious change on the structural relief between the western monocline and eastern monocline. Based on this observation, I suggest that there is no significant E-W shortening change across the Gallina-Archuleta arch.

6. Discussion

6.1 'Accommodation Zone' Model of Hamilton (2009)

The kinematic interpretation of Laramide deformation in north-central New Mexico is heavily debated because of the complex structures observed. In general, Laramide faults in north-central New Mexico show diffuse patterns that probably reflect the inclusion of differently oriented thrust, dextral, and even normal faults. However, the clustered Laramide folds and arches are a good indicator of Laramide horizontal shortening and compression directions (Erslev and Koening, 2009). These Laramide folds and arches are thrust-related folds; either fault-propagation or fault-bend folds. Therefore, the folds represent a thrust fault subset of Laramide structures. Based on the shortening and compression direction perpendicular to these thrust fault, arch, and fold orientations, researchers increasingly agree that the Nacimiento and Gallina uplifts result primarily from horizontal shortening (Yin and Ingersoll, 1997; Pollock et al., 2004; Erslev and Koening, 2009; Hamilton, 2009; Davis, 2010).

Based in part on the censuses of the regional Laramide horizontal shortening, Hamilton (2009) proposed an 'Accommodation Zone' model in which much of the strain in the Nacimiento uplift was transferred northeastward to the Tusas Mountains. This model predicted a significant change in the E-W shortening between the northern end of the Nacimiento uplift and the Gallina uplift. Davis (2010) calculated the E-W shortening across the bend area between the Nacimiento uplift and the Gallina uplift and concluded that the E-W shortening decreases from ~5 km at the northern end of the Nacimiento uplift to ~1 km along the Gallina uplift supporting Hamilton's (2009) interpreted transfer

zone. In regards to the calculations of Davis (2010), his line-length balancing of a cross section at the bend area between the Nacimiento uplift and the Gallina uplift (Figure 28) yielded 1.15 km of the E-W shortening. While Davis (2010) interpreted there to be two monoclines at the northern end of the Nacimiento uplift, similar to my results, he interpreted the western monocline to gradually die out to the north with only the eastern monocline continuing into the Gallina uplift. This is not consistent with published geologic maps and cross sections or my own results.

In this study my 3D model shows the eastern and western monoclines at the northern end of the Nacimiento uplift both extend to the Gallina-Archuleta arch which are consistent with the structures on published maps. Davis (2010) calculated the shortening across two monoclines at the northern end of the Nacimiento uplift but only calculated the shortening across the eastern monocline along the Gallina uplift. My shortening calculation (~5.3 km) is consistent with Davis' (2010) calculation (~5 km) across the northern end of the Nacimiento uplift. Within the Gallina uplift, my shortening calculation across the eastern monocline (~1.7 km) is a little larger than the calculation of ~ 1 km of Davis (2010). However, the calculations of Davis (2010) failed to take into account the westernmost monocline which adds another ~2.6 km of shortening. Integrating the shortening calculation from Pollock et al. (2004) with my results (Figure 29) shows there is only a slight change in shortening from the Nacimiento uplift to the Gallina-Archuleta arch. Thus, this study does not support Hamilton's (2009) prediction that significant E-W shortening was transferred from the northern end of the Nacimiento uplift to the southern end of the Tusas uplift.

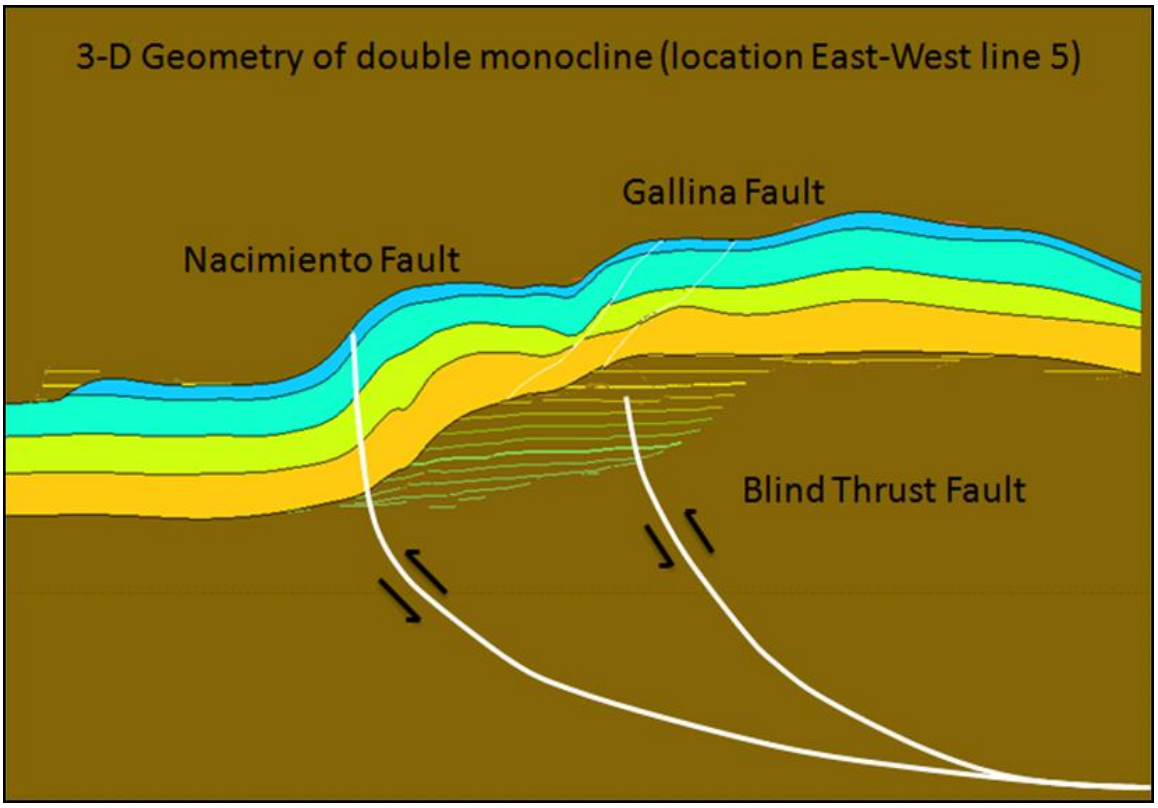

Figure 28. Interpreted cross section from Davis (2010) showing the subsurface geometry of the bend area between the Nacimiento uplift and the Gallina uplift.

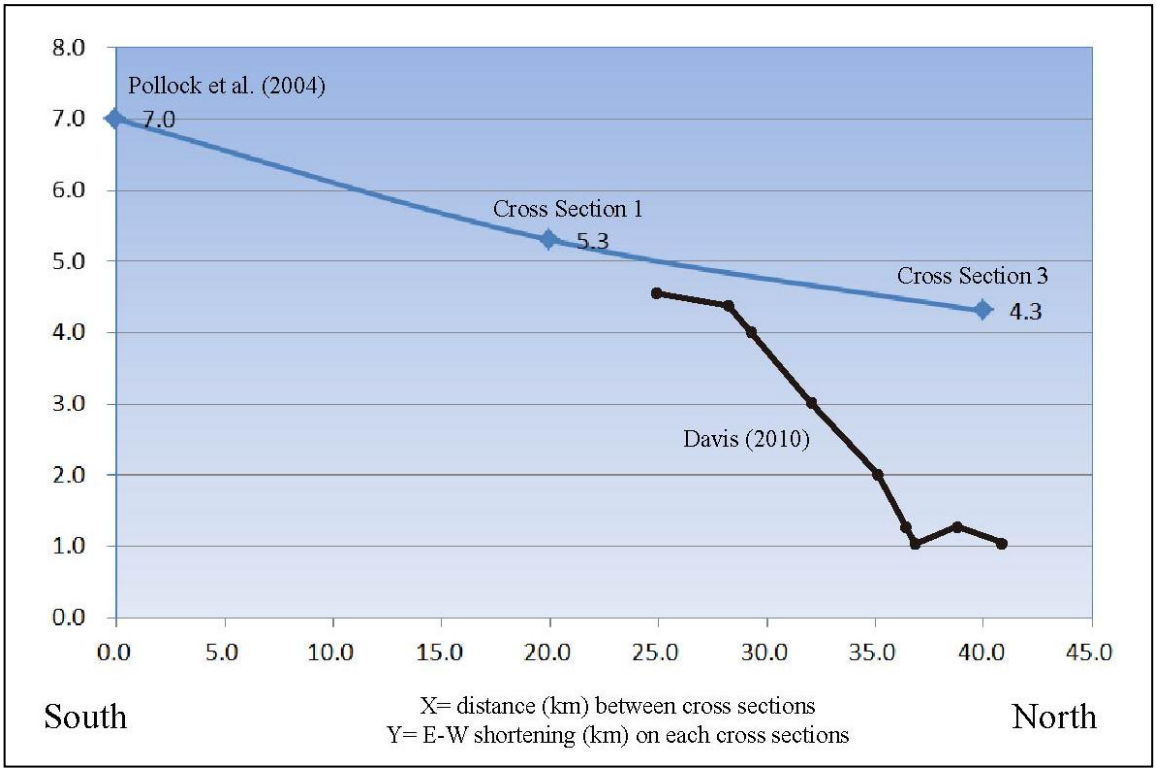

Figure 29. Graph showing the E-W shortening change from south at the central portion of Nacimiento uplift (Pollock et al., 2004) to north at the Gallina uplift. The black line is the shortening calculations from Davis (2010).

6.2 Kinematic Model of Laramide Deformation in North-Central New Mexico

The shear structures observed by Hamilton (2009) between the Nacimiento uplift and the Tusas uplift are parallel to the Tijeras-Canoncito fault to the south which was interpreted to identify the Laramide compressional direction by Yin and Ingersoll (1997). The orientation of the shear structures is also consistent with the average Laramide slip and maximum compressive stress directions (N67E) from Erslev and Koening (2009). Further, along the Nacimiento uplift minor shear fracture data and rose diagrams (Figure 5) of slickenline trends show unimodal, ENE-WSW-directed compression (Erslev, 2001). Therefore, the data indicate the Nacimiento uplift results from unidirectional and one phase ENE-WSW compression.

In this study I calculated an E-W component of shortening of ~5 km at the northern end of the Nacimiento uplift. Based on this calculation, the shortening along predicted compressive direction (N67E) by Erslev and Koening (2009) is ~5.4 km (5 km/sin67 °). A key observation is that this shortening is consistent with the length of the two high-angle ENE-WSW-striking faults (Figure 7) at the bend area between the Nacimiento uplift and the Gallina uplift. I suggest that these two faults are dextral strike-slip faults which are the northern boundary of the Nacimiento uplift. The western ENE-WSW-striking fault then bends to the NNE and connects with the Gallina fault.

ENE-WSW-directed shortening of ~5.4 km would produce a N-S component of shortening of ~2.1 km (~5.4 km/cos67 °). I suggest that this strain is accommodated by the Gallina fault, the NNE-SSW-striking subvertical fault observed to alternates from west-down to east-down along its trace (Baltz, 1967; Woodward et al., 1992). In the

Gallina uplift, rose diagrams of ideal σ_1 axes derived from fault slip vectors show a broad distribution between E-W and NNE-SSW trends (Erslev 2001) and Erslev and Koening (2009) indicated the kinematic interpretation of these structures requires three-dimensional strain compatibility. Therefore, I suggest that in the Gallina uplift the N67E stress decomposes into two directions. One is an E-W compression and resulted in the Gallina uplift. The other is in a NNE-SSW direction along the Gallina fault. The NNE-SSW compression is partly consistent with the kinematic model (Figure 3) used by Cather (2004) to interpret the formation of the San Juan basin axis and a series of en echelon folds on the eastern boundary of the San Juan basin. In my model (Figure 30) the Gallina fault is interpreted as a dextral strike-slip fault with ~2 km of displacement which accommodates the N-S component of shortening from the Nacimiento uplift. The dextral offset of ~2 km is also consistent with the measured separation between the axis of the San Juan basin and the axis of a broad syncline which connects the northeastern part of the Nacimiento uplift with the Chama basin (Figure 7).

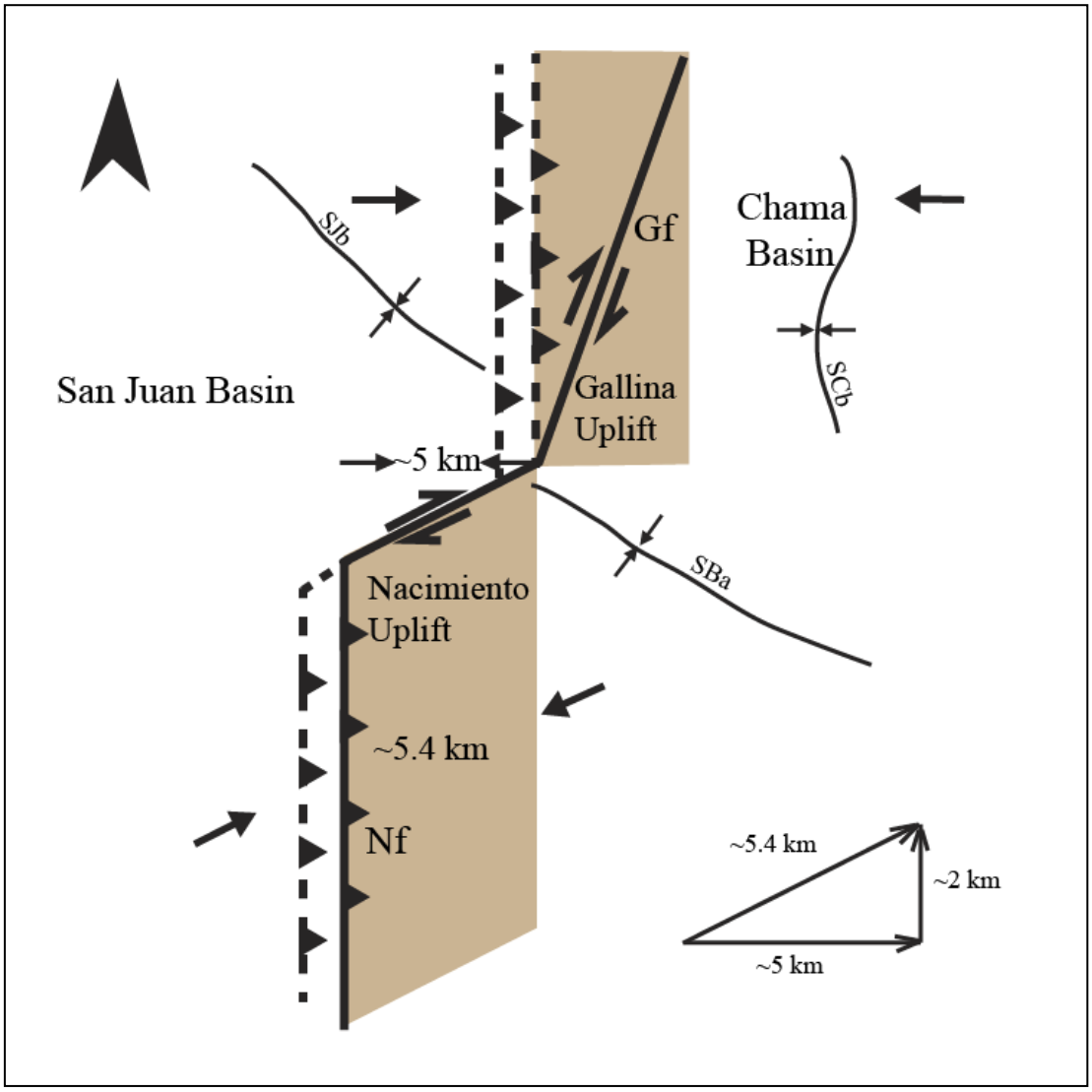

Figure 30. Simplified kinematic model of Laramide deformation in north-central New Mexico. SBa, axis of the bend area; SCb, axis of the Chama basin; SJb, axis of the San Juan basin; Gf, Gallina fault; Nf, Nacimiento fault.

7. Conclusion

Deformation related to the Late Cretaceous-Early Eocene Laramide orogeny in north-central New Mexico resulted in the formation of the Nacimiento uplift, Gallina uplift, and corresponding faults. Based on the 3D structural surface construction along the Nacimiento-Gallina uplifts, and forward modeling the formation of these structures based on the assumption the structures are fault-propagation folds, this study concludes the following:

First, the Nacimiento uplift consists of a western monocline and an eastern monocline. The western monocline results from a blind low-angle trust fault and the eastern monocline is the result of the high-angle Nacimiento fault. Modeling is consistent with the previous interpretation that the high-angle Nacimiento fault branches from the low-angle fault (Pollock et al., 2004).

Second, E-W shortening across the northern end of the Nacimiento uplift is ~5.3 km, consistent with the results from Davis (2010). The total E-W shortening decrease to ~4.3 km across the Gallina uplift as the Nacimiento fault becomes to blind beneath the eastern monocline. Integrating the E-W shortening calculation of ~7 km from Pollock et al. (2004), my results show there is no abrupt change on the E-W shortening between the Nacimiento uplift and the Gallina uplift in contrast to the results of Davis (2010) which found an abrupt decrease on the E-W shortening from the Nacimiento uplift to the Gallina uplift. Therefore, this study does not support the predication of Hamilton (2009) that significant E-W shortening was transferred from the northern end of the Nacimiento uplift to the Tusas uplift.

Third, I suggest that the maximum stress of N67E decomposes into two directions (E-W and NNE-SSW) in the Gallina uplift. Here, the E-W shortening is accommodated by the fault propagation folds, while the NNE-SSW-striking Gallina fault is interpreted as a dextral strike-slip fault with a displacement of ~2 km which accommodates the N-S component of shortening from the Nacimiento uplift.

8. References

Allmendinger, R.W., 1998, Inverse and forward numerical modeling of trishear fault propagation folds: Tectonics, v. 17, no. 4, p. 640-656.

Allmendinger, R.W., 2000, Estimation of fault-propagation distance form fold shape: Implication for earthquake hazards assessment: Geology, v. 28, no. 12, p. 1099-1102.

Allmendinger, R.W., Zapata, T., Manceda, R., and Dzelalija, F., 2004, Trishear kinematic modeling of structures, with examples from the Neuquen Basin, Argentina, in K.R. McClay.ed., Thrust Tectonics and Hydrocarbon Systems: AAPG Memoir 83, p. 356-371.

Baltz, E.H., 1967, Stratigraphy and regional tectonic implications of part of upper Cretraceous and Tertiary rocks East-Central San Juan basin New Mexico: Geological Survey Professional Paper, United States Government Printing Office, Washington, p. 1-101.

Brister, B.S., and Chapin, C.E., 1994, Sedimentation and tectonics of the Laramide San Juan Sag, southwestern Colorado: The Mountain Geologist, v. 31, no. 1, p. 2–18.

Cather, S.M., 1999, Implications of Jurassic, Cretaceous, and Proterozoic piercing lines for Laramide oblique-slip faulting in New Mexico and rotation of the Colorado Plateau: Geological Society of America Bulletin, v. 111, p. 849-868.

Cather, S.M., 2004, The Laramide orogeny in central and northern New Mexico and southern Colorado, in Mack, G.H., and Giles, K.A., eds., The Geology of New Mexico, A Geological History: New Mexico Geological Society Special Publication 11, p. 925-928.

Cather, S.M., Karlstrom, K.E., Timmons, J.M., and Heizler, M.T., 2006, Palispastic reconstruction of Proterozoic basement-related aeromagnetic features in north-central New Mexico: Implications for Mesoproterozoic to Late Cenozoic tectonism: Geosphere, v. 2, p. 299-323.

Chapin, C.E., and Cather, S.M., 1981, Eocene tectonics and sedimentation in the Colorado Plateau-Rocky Mountain area, in Dickinson, W.R. and Payne, W.D., eds., Relation of tectonics to ore deposits in the southern Cordillera: Arizona Geological Society Digest, v. 14, p. 173-198.

Chapin, C.E., 1983, Rocky mountain foreland basins and uplifts: Rocky Mountain Association of Geologists, p. 33-56.

Crouse, D.L., Michale, C.H., and Woodward, L.A., 1992, Geologic Map of French Mesa Quadrangle, Rio Arriba County, New Mexico; Department of Geology, University of New Mexico, Albuquerque, NM 87131: New Mexico Bureau of Mines & Mineral Resources, Geologic Map 67, scale 1:24,000.

Davis, P.S., 2010, Kinematics of the Nacimiento and Gallina uplifts in north-central New Mexico in relation to the Laramide tectonic evolution during the Late Cretaceous to Early Eocene, MS Thesis, University of Houston.

DeCelles, P.G., 2004, Late Jurassic to Eocene evolution of the Cordilleran thrust belt and foreland basin system, Western U.S.A. American Journal of Science, v. 304, p. 105-168.

Erslev, E.A., 1991, Trishear fault-propagation folding. Geology, v. 19, p. 617-620.

Erslev, E.A., 2001, Multistage, multidirectional Tertiary shortening and compression in North-Central New Mexico: GSA Bulletin, v. 113, no. 1, p. 63-74.

Erslev, E.A., and Koenig, N.V., 2009, Three-dimensional kinematics of Laramide basement-involved Rocky Mountain deformation, USA: Insights from minor faults and GIS-enhanced structure maps, in Kay, S.M., V.A. Ramos, and W.R. Dickinson, W.R. eds., Backbone of the Americas: Shallow Subduction, Plateau Uplift, and Ridge and Terrane Collision: The Geological Society (London) Memoir, v. 204, p. 125-150.

Fassett, J.E., and Hinds, J.S., 1971, Geology and Fuel Resources of the Fruitland Formation and Kirtland Shale of the San Juan Basin, New Mexico and Colorado: U.S. Geological Survey, Professional Paper 676, 76p.

Fassett, J.E., and Steiner, M.B., 1997, Precise age of C33N-C32R magnetic-polarity reversal, San Juan Basin, New Mexico and Colorado: New Mexico Geological Society, 48th Field Conference, Guidebook, p. 239–247.

Fassett, J. E., 2000, Geology and coal resources of the Upper Cretaceous Fruitland Formation, San Juan Basin, New Mexico and Colorado, *in* Kirschbaum, M.A., Roberts, L. N. R., and Biewick, L. R. H., eds., Geologic Assessment of Coal in the Colorado Plateau: Arizona, Colorado, New Mexico and Utah: U.S. Geological Survey, Professional Paper 1625-B, p. Q1–Q132.

Giral, R.A., 1995, Early structural evolution of a Laramide uplift, Sierra Nacimiento, New Mexico: Unpublished M.S. thesis, University of North Carolina at Chapel Hill, 53 p.

Hardy, S., Ford, M., 1997. Numerical modeling of trishear fault propagation folding. Tectonics, v. 16, no. 5, p. 841-854.

Hamilton, J., 2009, Low temperature thermal history of the Brazos uplift, New Mexico, MS Thesis, University of Houston.

Karlstrom, K.E., and Daniel, C.G., 1993, Restoration of Laramide right lateral strike slip in northern New Mexico using Proterozoic piercing points: tectonic implications from the Proterozioc to the Cenozoic: Geology, v. 21, no. 12, p. 1139-1142.

Kelley, V.C., 1955, Regional Tectonics of the Colorado Plateau and the Relationship to the Origin and Distribution of Uranium: University of New Mexico, Publications in Geology, no.5, 122 p.

Kelley, V.C., and Clinton, N.J., 1960, Fracture Systems and Tectonic Elements of the Colorado Plateau: Albuquerque. University of New Mexico Press, 104 p.

Kelley, S.A. and Chapin, C.E., 1995, Apatite fission-track thermochronology of Southern Rocky Mountain-Rio Grande rift-western high plains provinces: New Mexico Geological Society, 46th Field Conference, Guidebook, p. 87–96.

Landis, E. R. and Dane, C. H., 1967, Geologic Map of Tierra Amarilla Quadrangle, Rio Arriba County, New Mexico: New Mexico Bureau of Mines and Mineral Resources, Geologic Map 19, scale 1:62,500.

Laughlin, A.W., Eddy, A.C., and Laney, R., 1983, Geology of the Fenton Hill, New Mexico, Hot Dry Rock site : Journal of Volcanology and Geothermal Research, v. 15, no. 1-3, p. 21-41.

Mitra, S., 1990, Fault-propagation folds: geometry, kinematic evolution, and hydrocarbon traps. American Association of Petroleum Geologists Bulletin, v. 74, p. 921–945.

Merrick, M.A. and Woodward, L.A., 1982, Geologic Map of Regina Quadrangle, Rio Arriba and Sandoval Counties, New Mexico: New Mexico Bureau of Mines & Mineral Resources, Geologic Map 46, scale 1:24,000.

Pollock, C.J., Stewart, K.G., Hibbard, J.P., Wallace, L., and Giral, R.A., 2004, Thrust-wedge tectonics and strike slip faulting in the Sierra Nacimiento, New Mexico, in Cather, S.M., McIntosh, W.C., and Kelley, S.A, eds., Tectonics, Geochronology, and Volcanism in the Southern Rocky Mountains and Rio Grande Rift: Socorro, New Mexico Bureau of Geology and Mineral Resources, Bulletin, v. 160, p. 97–111.

Reeves, S., and Billingsley, R., 2002, Stratigraphic chart of eastward San Juan basin reproduced from Bureau of Indian Affairs, Atlas of Oil and Gas Plays on American Indian Lands; Jicarilla Apache Indian Reservation, New Mexico in Application of Advanced Exploration Technologies for the Development of Mancos Formation Oil Reservoirs, Jicarilla Apache Indian Nation, San Juan Basin, New Mexico, 15 p.

Renick, B.C., 1931, Geology and Ground-water Resources of Western Sandoval County, New Mexico: U.S. Geological Survey, Water-Supply Paper 620, 117 p.

Sikkink, P.G.L., 1987, Lithofacies relationships and depositional environment of the Tertiary Ojo Alamo Sandstone and related strata, San Juan Basin, New Mexico and Colorado, in Fassett, J. E. and Rigby, J. K., Jr., eds., The Cretaceous-Tertiary Boundary in the San Juan and Raton Basins, New Mexico and Colorado: Geological Society of America, Special Paper 209, p. 81–104.

Slack, P.B., and Campbell, J.A., 1976, Structural geology of the Rio Puerco fault zone and its relationship to central New Mexico tectonics, in Woodward, L.A. and Northrop, S. A., eds., Tectonics and Mineral Resources of Southwestern North America: New Mexico Geological Society, Special Publication 6, p. 46–52.

Stewart, K.G., and Hibbard, J.P., 1992, Low angle thrust faulting at the eastern edge of the San Juan Basin associated with the Nacimiento uplift; in Lucas, S.G., Kues, B.S., Williamson, T.E., and Hunt, A.P. (eds.), San Juan Basin IV: New Mexico Geological Society, Guidebook 43, p. 7–9.

Suppe, J., and Medwedeff, D.A., 1990. Geometry and kinematics of fault-propagation folding: Eclogae Geologicae Helvetiae, v. 83, p. 409-454.

Woodward, L.A., 1974, Tectonics of Central-Northern New Mexico: New Mexico Geological Society Guidebook, 25th Field Conference, Ghost Ranch (Central-Northern N.M.), p. 123-129.

Woodward, L.A., 1976, Laramide deformation of the Rocky Mountain foreland; geometry and mechanics, in Woodward, L. A., and Northrop, S. A., eds., Tectonics and Mineral Resources of Southwestern North America: New Mexico Geological Society Special Publication 6, p. 11–17.

Woodward, L.A., 1987, Geology and Mineral Resources of Sierra Nacimiento and vicinity, New Mexico: New Mexico Bureau of Mines and Mineral Resources, Memoir 42, p. 7-84.

Woodward, L.A., Hultgren, M.C., Crouse, D.L., and Merrick, M. A., 1992, Geometry of the Nacimiento-Gallina fault system, northern New Mexico, in Lucas, S. G., Kues, B., S., Williamson, T. E., and Hunt, A. P., eds., San Juan Basin IV: New Mexico Geological Society Guidebook 43, p. 103–108.

Woodward, L.A., 1996, Paleotectonics of the late Paleozoic Peñasco uplift, Nacimiento region, northern New Mexico, in Goff, F., Kues, B. S., Rodgers,M. A. McFadden, L. D., and Gardner, J. N., eds., The Jemez Mountains Region: New Mexico Geological Society Guidebook 47, p. 107–113.

Woodward, L.A., Anderson, O.J., and Lucas, S.G., 1997, Mesozoic stratigraphic constraints on Laramide right slip on the east side of the Colorado Plateau: Geology, v. 25, p. 843–846.

Yin, A., and Ingersoll, R.V., 1997, A model for evolution of Laramide axial basins in the southern Rocky Mountains, U.S.A.: International Geology Review, v. 39, p. 1113-1123.